ÓBUDAI EGYETEM
ÓBUDA UNIVERSITY

DOCTORAL (PHD) THESIS

GÁBOR JÁNOS MANHERTZ

Hybrid Evaluation Method for Rotating Machine Transient Vibration Analysis Using Signal and Image Processing Methods

Supervisor:
Károly Széll, PhD
Óbuda University, Alba Regia Technical Faculty,
Székesfehérvár

DOCTORAL SCHOOL OF
APPLIED INFORMATICS AND
APPLIED MATHEMATICS

29th December 2021, Budapest

Szigorlati bizottság:

Elnök: Prof. Dr. Tar József

Tagok: Dr. Budai Csaba, Dr. Vörös András

Nyilvános védés teljes bizottsága:

Elnök:

Tagok:

Titkár:

Nyilvános védés időpontja:

Doktori disszertációmat Mamának és Apának (✝) ajánlom.

Nyilatkozat a munka önállóságáról

Alulírott *Manhertz Gábor János* kijelentem, hogy a *Hybrid Evaluation Method for Rotating Machine Transient Vibration Analysis Using Signal and Image Processing Methods* című benyújtott doktori értekezést magam készítettem, és abban csak az irodalmi hivatkozások listáján megadott forrásokat használtam fel. Minden olyan részt, amelyet szó szerint, vagy azonos tartalomban, de átfogalmazva más forrásból átvettem, a forrás megadásával egyértelműen megjelöltem.

Budapest, 2021. 12. 29.

. . . .

Manhertz Gábor János

Köszönetnyilvánítás

A doktori kutatási tevékenységemet 2013 tavaszán kezdtem. Több alkalommal is akadályok gördültek elém, de végül mindig újult erővel igyekeztem eljutni a kívánt célig. Ennek eredményeképp született meg jelen disszertáció, melyet sokak nélkül biztosan nem értem volna el.

Szeretnék először és legfőképpen köszönetet mondani Édesanyámnak és Édesapámnak, akik elindítottak a mérnöki pálya felé. Mindig támogattak abban, amit csinálok, amit el akarok érni és mindig emlékeztettek arra, hogy nem céltalan az egész tevékenység - hiszen a végén a befektetett energia megtérül. Apa sajnos pár hónap híján, de nem élhette meg személyesen ezt velem, de ettől függetlenül tudom, hogy büszke lenne. Nélkülük nem tartanék ott ahol. Köszönöm Testvéremnek, hogy megmutatta, lehet nagyot alkotni egy doktori disszertációval, hiszen ő is megszerezte ezt a tudományos címet egy igazán nívós munkával.

Szeretnék köszönetet mondani Páromnak, aki bár sokszor szóvátette, hogy miért "kínzom" magam, de mindvégig támogatva állt mellettem. Köszönettel tartozom barátaimnak Mátyinak, Levinek, Gikának és sokan másoknak, akik támogattak mindig is.

Hálásan köszönöm Dr. Lipovszki Györgynek, hogy megkedveltette velem a LabVIEW programozást; Dr. Pór Gábornak, hogy bevezetett a műszaki diagnosztika rejtelmeibe, valamint Dr. Bereczky Ákosnak, hogy mentorként vitt be a belsőégésű-motorok világába, ahol az eddig elsajátított tudományágak egy szeletét alkalmazhattam. Köszönöm a tartalmas beszélgetéseket, valamint a lehetőséget, hogy méréseket végezhettem. Továbbá köszönöm a BME MOGI Tanszéknek az ott töltött kutatási éveket, a tartalmas munkát és beszélgetéseket.

Köszönöm a Vincotech Hungária Kft. R&D Application Concept & Product Development csapatának, hogy támogatták a teljesállású munka mellett a doktori tevékenységemet.

Végül, de nem utolsó sorban nagyon nagy köszönettel tartozom Dr. Széll Károlynak, témavezetőmnek, aki rendíthetetlenül noszogatott és figyelt arra, hogy ez a dolgozat megfelelő tartalommal és minőségben készüljön el.

Contents

List of Acronyms

AS	Amplitude Spectum. 18, 19
ASD	Amplitude Spectral Density. 21
BCG	Brightness-Contrast-Gamma. 44, 49, 73, 79
CM	Condition Monitoring. 2
CWT	Continous Wavelet Transform. 24
DFT	Discrete Fourier Transform. 7, 8, 13, 15–17, 19, 23–27, 73
DTM	Differential Tracking Method. 54, 96
DUT	Device Under Test. 9, 10
DWT	Discrete Wavelet Transform. 24
EMD	Empirical Mode Decomposition. 8
ENBW	Equivalent Noise-power Bandwidth. 21, 23
FD	Frequency Domain. 3, 7, 8, 13, 14, 23
FFT	Fast Fourier Transform. 8, 13, 17–19, 21, 24, 32, 33, 36, 37
FGV	Functional Global Variable. 33
FPGA	Field-Programmable Gate Array. 80
FT	Fourier Transform. 7, 8, 13, 15, 23, 24, 27–29, 31

GWN	Gaussian White Noise. 36
HHT	Hilbert-Huang Transform. 8, 23
ICE	Internal Combustion Engine. 8, 9, 11, 35, 68
LMD	Local Mean Decomposition. 8
MAPTM	Moving-Average-Predictive Tracking Method. 56–58, 74, 96
OBD	On-Board Diagnostics. 12
PS	Power Spectum. 18, 21
PSD	Power Spectral Density. 21, 30
RMS	Root Mean Square. 4–7, 18, 19, 34
RPM	Rotation Per Minute. 9, 10, 23, 34–36, 50, 75
SNR	Signal-to-Noise Ratio. 21, 34, 35, 68, 69, 76
STFT	Short-Time Fourier Transform. 8–11, 13, 14, 23–28, 30–33, 37, 41, 50, 53, 55, 62, 65, 69, 73, 75, 76, 79, 80
TD	Time Domain. 3, 4, 7, 13, 14
TF	Time-Freuqency. 34, 41, 58, 64, 69, 74, 75
TFD	Time-Frequency Domain. 3, 8, 10, 13, 24
THD	Total Harmonic Distortion. 34
TQM	Total Quality Maintenance. 9
UWN	Uniform White Noise. 36

VFR-STFT	Variable Frequency Resolution Short-Time Fourier Transformation. 79
WD	Wigner-Ville Distribution. 8
WPT	Wavelet Packet Transform. 24
WT	Wavelet Transform. 8, 23, 24

List of Symbols

Sign	Description	Unit
A	Spectral amplitude	$\frac{\mathrm{V}^2}{\mathrm{Hz}}$
K, M, n, i	Integer running variables	
M	Lenght of a discrete-time series	
N	Number of samples	pcs
$P_{i+1,j}$	Coordinates of a detected frequency point on the image	pixel
$P_{i,j}(x_{i,j}; y_{i,j})$	Coordinates of an image point	pixel
P	Energy consumption	kW
T	Wavelet transformation parameter	
V_{RMS}	Effective amplitude	
V_{pk}	Peak amplitude	
$\Delta\Phi$	Window bandwidth	dB
$\Delta\omega$	Frequency resolultion of a spectrogram	$\frac{\mathrm{rad}}{\mathrm{s}}$
Δ_{mesh}	Difference between two vertical mesh lines	pixel
Δ_{ω}	Angular frequency resolution	$\frac{\mathrm{rad}}{\mathrm{s}}$
Δ_f	Frequency resolution	Hz
Δ_t	Time resoluton of a signal	s
Δt	Time resolution of a spectrogram	s
Δ	Difference	
δ	Predictor value in the Predictive Tracking Method	pixel
$\hat{P}$	Closest found point	pixel
$\mathbf{D}$	Vector containing previous absolute minimum difference values	pixel
$\tilde{\mathbf{d}}$	Distance vector of the MAPTM method	pixel
$\mathbf{d}_n$	Distance on image between two detected points	pixel

Sign	Description	Unit
$\mathbf{d}$	Distance vector	pixel
$\mathbf{f}_k$	Vector of found points along a frequency line	pixel
$\gamma^*(\tau)$	Window functions	
$\psi(t)$	Mother wavelet	
$\mathrm{x}(t)$	STFT continous input signal	
$\mathrm{x}[n]$	Discretized STFT input signal	
ω	Angular frequency	$\frac{\mathrm{rad}}{\mathrm{s}}$
σ	Standard distribution	
$\tilde{\delta}$	Predictor value in the Moving-Average-Predictive Tracking Method	pixel
ε	Tolerance value	pixel
c_j	Gábor-transformation weighting coefficient	
$f_{\max}$	Maximum testable frequency in sampled signal	Hz
f_s	Sampling frequency	Hz
s	Wavelet scaling parameter	
t_{W}	STFT window length	s
t_f	End of the time signal under analysis	s
t	Time	s

Chapter 1

Introduction

Rotating machine diagnostics is a part of rotating machine maintenance evolving in a very diverse and dynamic way which increases the economic and reliability requirements.

As a result of technical progress, condition-dependent and comprehensive maintenance systems are coming at an accelerating pace. The rotating machines' specific parameters are evaluated based on regular or continuous monitoring and measurement from which the condition and remaining life of the machine are predicted. With this technique, it is possible to ensure that intervention is required for repairs only in those technically justified cases. However, at the same time, except for one sudden fault, sufficient time is available to prepare for repairs.

1.1 Rotating Machine Vibration Diagnostics

Vibration diagnostics is a particular branch of technical diagnostics that deals with measuring and evaluating an equipment's vibration response to dynamic forces. Vibration measurements and vibration-based diagnostic methods are often used in a wide range for rotating machines that have made these techniques considered universally approved and accepted tools for enhancing performance and safety [1]. Vibration diagnostics has several sub-areas and classifications like

1. Condition monitoring
2. Design optimization
3. Dynamic qualification

4. Seismic qualification

5. Machine installation and commissioning

6. Ageing management

7. Vibration isolation

During this research and thesis, the topic built around mainly the sub-area Condition Monitoring (CM) for which an example system can be seen in Fig. 1.1. The need for an effective CM and machinery maintenance program is reasonable wherever complex and expensive equipment is used to ensure business functions and value creation processes. Rotating machines are a central part of manufacturing procedures and our everyday lives, and their health and availability directly affect schedules, quality, and costs. Components, including motors, bearings, gearboxes, etc., are engaged to operate effectively to keep the rotating machine stable and healthy. For that reason, maintenance is performed by repairing, modifying, or replacing these components in order to ensure that machines remain in a healthy condition. [2]. Maintenance can be accomplished using two main approaches: corrective and preventive maintenance [3]. Vibration analysis can be suitable for both directions though the focus in this thesis is not to decide which maintenance method is more appropriate or efficient.

Besides different theoretical approaches and grouping, there are two standards dealing with vibration protection systems for high value rotating machines, which have to be mentioned [4]. The first one is the API 670 standard which describes the minimum requirements for Machinery Protection System (MPS) that measures general vibration information about the shaft and casing with supplement position, rotational speed, over-speed, and/or critical machine temperatures. The second one is the ISO 7919 which describes general requirements for measurement and evaluation of the vibration of different machine types when the vibration measurements are made on rotating shafts. The standard consists of multiple parts depending on the characteristics of the rotating machine.

The main focus of this work is to enhance vibration diagnostics or other science fields for rotary machinery with the usage and combination of well-known scientific methods and novel methods to open the possibility for the application in real environments.

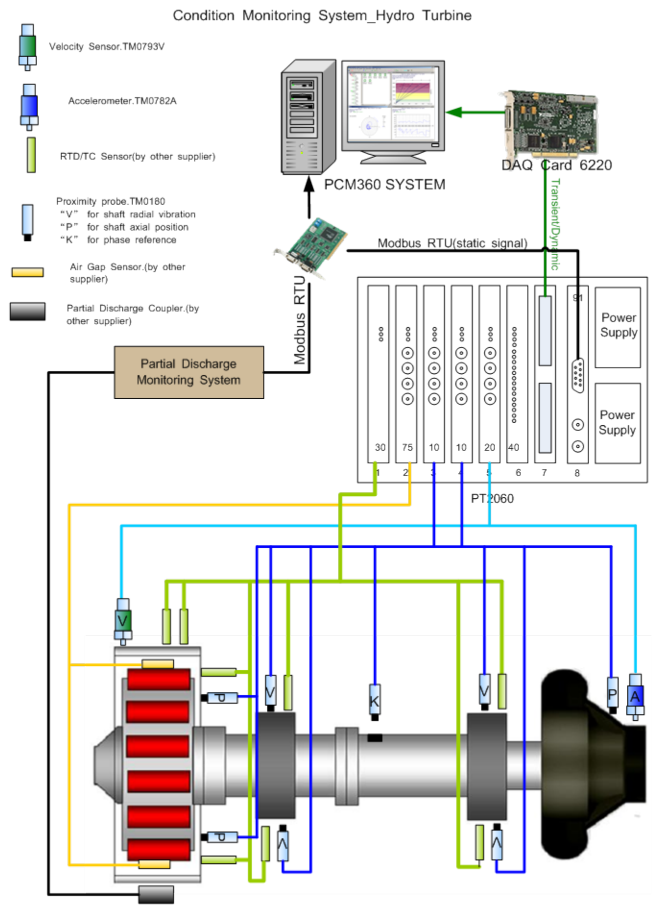

Figure 1.1: An example condition monitoring system (`www.pvtvm.com`)

1.2 Analysis of Stationary and Transient Signals

In order to introduce the main topic more deeply, fundamental vibration diagnostic theories and definitions have to be discussed.

Vibration is a periodic back-and-forth motion of the particles of an elastic body or medium, commonly resulting when almost any physical system is displaced from its equilibrium condition and allowed to respond to the forces that tend to restore equilibrium [5]. In order to process this physical phenomenon quantitative analysis is essential.

Nowadays, such data analysis is not unique and not a special case in the digital world. The previously mentioned quantitative data has to be measured and evaluated as a physical signal to achieve this. Signal processing is a key area of knowledge that finds applications in virtually all aspects of modern life. Signal processing consists of mapping or transforming information-bearing signals into another form of signals at the output. This mapping defines a continuous or analogue system if it involves functions representing the input and output signals. On the other hand, the system is discrete or digital if sequences of numbers represent its input and output signals. [6].

Such kinds of measured signals can be evaluated differently, with various methods providing diverse information about the machine under measurement. For analysing vibration, there are three leading groups which are generally accepted in the science - Time Domain (TD) analysis, Frequency Domain (FD) analysis and Time-Frequency Domain (TFD). The dimensional representation of these two approaches is illustrated in Fig. 1.2. The basis of this chapter is the first five chapter of [7].

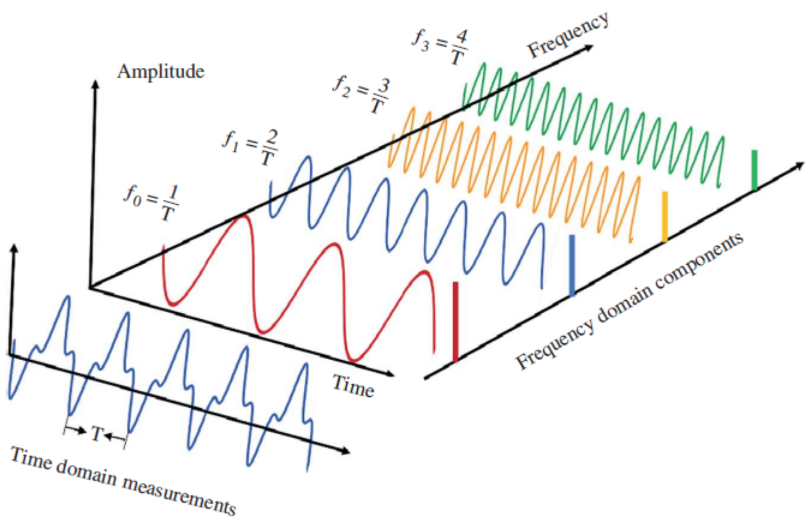

Figure 1.2: Illustration of Time Domain and Frequency Domain analysis [7]

The basics of the methods used in each group will be presented in the following subsections.

1.2.1 Time Domain Analysis

TD analysis is analysing the data over a time section. Electronic signals, market behaviours, and biological systems are some of the functions that are analysed using time domain analysis. For an electronic signal, the TD analysis is mainly based on the voltage-time plot or the current-time plot. In a time domain analysis, the variable is always measured against time. In the case of vibration measurements, time domain analysis mainly evaluates the measured vibration represented as voltage.

When the vibration time function is acquired, different vibration signal specific TD analysis methods can be applied to extract meaningful information about the machine's state. Some examples are represented in Table 1.1.

Table 1.1: Time Domain (TD) method groups with examples

Group	**Example method**
Basic and descriptive statistical values	• Peak • Peak-to-peak • Threshold • RMS • Crest factor • Mean • Mode • Median • Skewness • Variance • Kurtosis • Overall vibration • SPRT
Signal shape metrics	• Envelope • Dynamic threshold
Time function of basic and descriptive statistical values	• RMS(t) • Kurtosis(t)

The basic descriptive values are derived from the signal without any calculation or modification. These values are the peak and the peak-to-peak amplitude values. In order to extend the previously mentioned values, basic statistical descriptive values have to be introduced like Mean, Mode, Root Mean Square (RMS). The representation of these values can be seen in Fig. 1.3. The descriptive statistical analysis can be extended further with the variance; Skewness; Kurtosis – the statistical moments; standard deviation (at confidence levels 65.5%, 95% and 99.73%); median; and signal range. After the calculation, the histogram of the loaded data sequence and the numerical results are displayed. With the simple threshold test, the number of the signal peaks could be registered, which are higher than the set threshold levels that can have a negative or positive direction. Crest factor is also a well-known parameter of a waveform representing the ratio of the peak values and the effective values. As a general statement, if the signal distribution is tighter than the normal distribution then it concludes that the mean value and standard deviation could be the same [8, 9]. The equations below represent the calculation of some of the parameters mentioned above. These are the Crest factor (Eq. 1.1), Skewness (Eq. 1.2) and Kurtosis (Eq. 1.3).

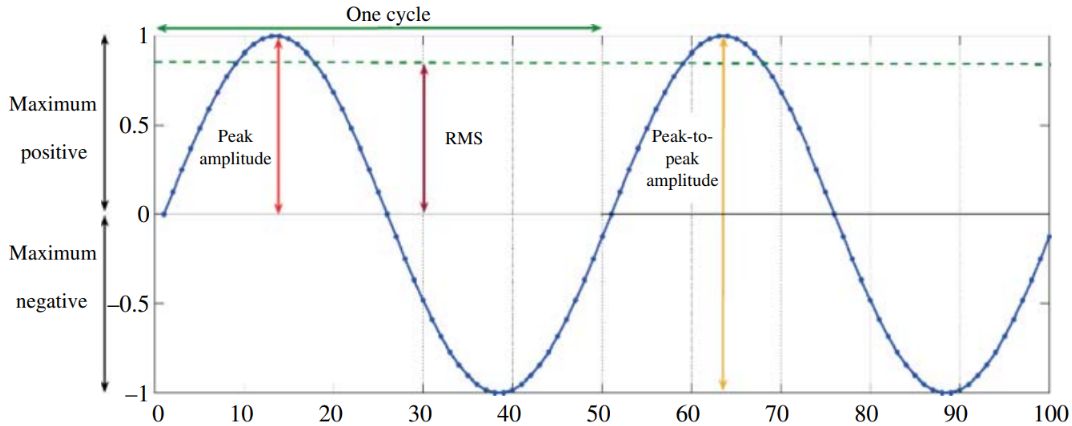

Figure 1.3: Illustration of signal descriptive values in Time Domain [7]

The Crest factor can be calculated by using

$$C = \frac{|x_{\text{peak}}|}{x_{\text{RMS}}}, \tag{1.1}$$

where x_{peak} is the absoluate peak and x_{RMS} is the RMS value of the time signal. The Skewness (third moment of a stochastic process) can be estimated by

$$\alpha_3 = \frac{\sum_{i=1}^{N}(x_i - \tilde{x})^3}{(N-1)\sigma^3}. \tag{1.2}$$

The Kurtosis (fourth moment of a stochastic process) can be estimated by

$$\alpha_4 = \frac{\frac{1}{N}\sum_{i=1}^{n}(x_i - \tilde{x})^4}{(\frac{1}{N}\sum_{i=1}^{n}(x_i - \tilde{x})^2)^2}. \tag{1.3}$$

where x are values in the signal, $\tilde{x}$ is the mean of the signal, N is the number of samples in the signal and σ is the standard deviation of the signal.

The Sequential Probability Ratio Test (SPRT) invented by [10] is a method which compares the probability density functions using the ratio of two conditioned probabilities. In the denominator, there is the probability which samples belong to a process with probability density of hypothesis H1, while in the nominator, we have the same probability, which samples belong to probability density of H0 hypothesis [8]

$$\lambda_n = \ln \frac{p(x_1, x_2, ..., x_n|H_1)}{p(x_1, x_2, ..., x_n|H_0)}. \tag{1.4}$$

The next group can be called signal shape metrics. The improvement of the simple threshold test, resulted in the dynamic threshold test, which allows us to fit an envelope of a given resolution to the signal. It can be observed at which time which part of the signal exceed these limits. This kind of simple envelope test can be useful, e.g. in production lines where a so-called "gold" product is measured. The resulted signal of that measurement could be the reference of this envelope test because the other products can be compared to this gold-reference [8, 11].

The final group worth mentioning is the time function creation of basic and descriptive statistical values. Let us take an example. In the time-dependent RMS calculations, such functions could be created, which basis was the simple RMS parameter mentioned in the descriptive statistical analysis. The first RMS method calculated the average RMS value without overlapping within a time-segment. From these results, a time-dependent RMS-average function has been constructed. The second method calculated the simple RMS value within a time-segment with overlapping. This resulted an RMS(t) function. The average of the RMS(t) function needed to be equal with the RMS value resulted in the statistical analysis. The width and the overlapping of the time-windows could be adjusted via input parameters. [8, 11]. Such a windowing-based time-function creation method can be applied on any kind of signal; the question is which parameter or scalar value will be the basis of the calculation - i.e. which value is calculated within a time segment.

A more in-depth description of the TD methods and their background can be found in Part II, Chapter 3 of [7].

1.2.2 Frequency Domain Analysis

FD analysis is widely used in fields such as control systems engineering, electronics and statistics for signals or functions that are periodic over time. However, this does not mean that frequency domain analysis cannot be used in signals that are not periodic.

Vibration signals in practice usually consist of various frequencies and their harmonics. It cannot be seen immediately by looking at the amplitude-time pattern how many components there are, and at which frequencies. When analysing machine vibrations, we usually find several prominent periodic frequency components directly related to the fundamental movements of various parts of the machine. With frequency analysis, we are therefore able to track down the source of undesirable vibration.

The frequency representations of these signals in the frequency domain are often performed using Fourier analysis which is generally classified into three types: Fourier series, Fourier Transform (FT), and Discrete Fourier Transform (DFT). The basic idea of Fourier analysis was discovered in the 19th century by the French mathematician J. Fourier which novum was that any periodic function could be expressed as a summation of complex exponential functions. From these types DFT is an important tool in the frequency analysis of discrete-time signals [12, 13].

More in-depth description about the FD methods and their background can be found in Part II, Chapter 4 and 5 of [7]. Different types of vibration signal specific FD analysis methods can be applied to extract meaningful information about the state of the machine. A primary grouping with some examples can be found in Table 1.2.

Table 1.2: Frequency Domain (FD) method groups with examples

Group	**Example method**
Frequency Domain Methods	• DFT • Fast Fourier Transform (FFT) • Frequency envelope • Higher-Order spectra • Cepstrum
Time-Frequency Domain Methods	• Short-Time Fourier Transform (STFT) • Wavelet Transform (WT) • Empirical Mode Decomposition (EMD) • Hilbert-Huang Transform (HHT) • Wigner-Ville Distribution (WD) • Spectral Kurtosis • Local Mean Decomposition (LMD)

The basis of this research is partially the FD and the TFD analysis, thus in accordance with this, more extensive mathematical details about the FT and the spectral representation types can be found in this thesis in Chapter 2.

1.3 State-of-the-Art

Nowadays, rotating machine manufacturers continuously try to adapt or precept directives of the competition on the market. The best compromise between the price, the operational safety, condition monitoring, the fuel consumption, the emission limits and the performance have to be considered, as the quality of the product. In order to manage this, the research and development activities are moving towards facing more automated and reliable solutions with which the measurement and analysis can give higher quality results. The main subject of this analysis could be the vibration of rotating machines and analyse the engine's vibration with several methods to provide a more reliable and safer operation in Internal Combustion Engine (ICE) and electrical drives, which are the necessary elements of a vehicle's drive chains today [14]. Vibration measurement is fundamental because production defects can be detected quick and accurate at the end of the production line.

To improve the manufacturing process, ensure the quality of the products, and reduce costs, it is essential to identify defective automotive parts. For manufacturing processes, several methods can increase the quality of the products and the process's reliability. A kind of the quality assurance is the Total Quality Maintenance (TQM) method discussed in [15]. It claims that implementing a vibration-based maintenance strategy provides possibilities for acquiring early indications of changes in machinery state, and the vibration-based condition monitoring solutions became popular in various industries.

Several methods can disclose defects during or after the manufacturing and assembling processes, such as on-line monitoring systems, off-line production parameter optimisation or quality assurance procedures [16–18]. A specialised measurement system can be found in [19] where measurements of vibration and acoustic emission are combined. Some of the condition monitoring systems use the measurement of vibration and/or emitted noise to classify healthy and defective products with high efficiency [20].

Different research works represent fundamental vibration-based case studies on a theoretical basis [21,22]. Alternatively, even as examples, articles have demonstrated the stabilising effect of dry friction in systems which are destabilised by the sampled-data nature of the applied controller [23–25]. The method was used later to test haptic devices [26,27]. The phenomenon can be further generalised to vibrations composed of several vibration components [28]. Vibration measurement is influential because production faults or malfunction can be detected fast and accurate. These studies apply the basics of vibration analysis which is frequently used in engineering practice in expert systems. Some part of these systems were sharpened for condition monitoring and fault diagnosis of rotating machines. Reference [29] represents a complex solution that can consider the analysis of multiple rotating elements in one construction using basic spectrum analysis or amplitude distribution.

Some of these systems are used for condition monitoring and fault diagnosis of rotary machines. In reference [30], a system is presented for engine fault diagnosis from the development procedure until the application. In condition monitoring tasks the Device Under Test (DUT) often operates with non-stationary Rotation Per Minute (RPM). To analyse ICE in this state, the basic time and frequency domain methods [31] are not quite suitable. Higher level methods like wavelet transform can be a proper method to obtain basic information about operational conditions; Wang [32] represents such research works. Besides wavelet transformation STFT and spectrogram based methods are also commonly used but not only in vibration diagnostics and condition monitoring. More research works represent that not only spectrogram analysis in a traditional way can be a good base for vibration and sound analysis to obtain information but the proper combination of the data evaluation with other research fields. The expert systems in [33, 34] can be used mainly for condition monitoring and malfunction detection. In the case of condition monitoring tasks the DUT operates with non-stationary speed (RPM), so in order to analyse rotating machines in this transient state the elementary TFD methods [35] are not appropriate. For RPM estimation [36] represents a novel method which can be used for rotary machines. Multiple directions could be appropriate for this estimation like vibration spectra or cepstra, the advantages and disadvantages of which are described in [37].

Vibration analysis is applied frequently as the basis of expert systems. Some of these systems are used for condition monitoring, and fault diagnosis of electrical motors [38]. Frequency-based failure analysis is often used to investigate both motors [39] and the attached couplings [40]. A higher level of computer intelligence could be implemented in these systems with the use of neural networks [41]. Neural networks gain more space in expert system applications tailored for analysing rotating machines along different conditions [42, 43]. The combination of the statistical quality control, the vibration analysis [44] can result in a highly automated and controlled manufacturing process in the future. Vibration-based measurement systems became very common in the industrial environment nowadays. In reference [45], the generic methodology to develop an intelligent monitoring system for machining processes is described, presenting the benefits of using the vibration measurement in such a system. Yu et al. in [46] represents a vibration measurement experiment based on the Gaussian mixture model to detect bearing faults after assembly. In reference [47], a mathematical model based on the response surface-based D-optimal design is proposed for modelling and analysing tool vibration and surface roughness in the precision end-milling process. A real-time implementation of commonly used vibration features (peak amplitude, root mean square etc.) can be found in [48]. Nowadays, Industry 4.0 solutions are gaining more and more weight, therefore at larger manufacturers (e.g. SKF or Schaeffler) the integration of vibration diagnostics solutions is a priority research and development topic. References [49–51] represent such kind of realized applications, research directions and results.

Using a higher level method, like Wavelet-transformation, could be a suitable method to obtain factual information about operational conditions [52, 53]. A review containing the utilisation of wavelets for fault diagnosis can be found more detailed in [54]. Besides Wavelet-transformation the STFT-based methods are also applied frequently [55–58] as well but not only exclusively for vibration diagnostics and condition monitoring.

In case of the spectrogram it could be an approach to use image evaluation and processing methods. Reference [59] uses STFT for image to sound conversion. Zhang et al. [60] operates with the STFT to analyse diffractions. In the condition monitoring of ICEs obviously the spectral components on the STFT spectrogram need to be tracked or extracted. Markov models [61] and image processing [62] were also research guidelines in order to perform this action. [63] represents new guidelines in spectrogram image processing, which can be the basis of this and further research works. Besides these, references [64] and [65] describes new research methods in condition monitoring based on spectrograms and image processing presented before. In addition to these, [66–70] describe research initiatives and reviews for condition monitoring based on time-frequency domain, spectrograms and image processing with the extension of tracking methods.

Further researches in literature represent that the traditional spectrogram analysis is not the only suitable way for information extraction. In the case of spectrograms, it could be straightforward to apply image evaluation, and processing methods [71]. For condition monitoring of rotating machines, the possibility can be opened to track spectral components on a STFT spectrogram. The signal's resolution can influence this kind of analysis, and the STFT spectrogram [72].

1.4 Thesis Outline

This research aims to analyse and measure transient vibration signals in a non-laboratory environment acquired by industrial vibration sensor mounted on rotating machines. The combination of multiple disciplines in measurement and analysis could enhance the information extraction from vibration measurements in case of transient signals. The extracted information can be used to support more detailed vibration post- or real-time diagnostics of rotating machines during transient states by providing the primary, pre-processed time-frequency information.

The transient analysis is an essential criterion as rotating machines are primarily used during variable operational states; therefore, the reaction of the construction elements under variable circumstances needs to be observed. The industry moves towards alternative drives, so besides ICE, hybrid and purely electric drives begin to gain much more focus. For this reason, electric motors needed to be kept in mind while conducting the research. A standard industrial vibration sensor is always mounted on the rotating machine during the manufacturing process, and its signal can be used for measurements in a non-laboratory environment. On the other hand, this sensor's cost-effective application enables to obtain operational conditions about the construction. However, high-frequency ranges could not be adequately analysed due to the bandwidth (30 Hz - 25 kHz) of this type of sensor. There is a possibility of end-of-line transient testing of the mechanical construction itself after manufacturing or using on-board diagnostics after signal evaluation and preparation obtaining the signal via e.g. On-Board Diagnostics (OBD) protocol. Therefore, the information could be collected about the rotating machine's stationary and transient behaviours during manufacturing tests or daily usage, which could be utilised for predictive maintenance or malfunction detection.

In summary, we are looking for a method with the capability to analyse in low and mid-frequency ranges the stationary and transient vibration measurements derived from rotating machines using an industrial vibration sensor. This research was inspired by a study cited in [73] containing the combination of multiple disciplines such as signal and image processing. The research aimed to extend the signal processing part and define a more efficient and scalable method to support the input of rotating machine diagnostics.

Chapter 2

Spectrogram Creation

In the first section of Chapter 2 a more detailed introduction of FD signal analysis methods are introduced. The description starts from the basic FT introducing the spectrum types and some of the fundamental window types. This will be followed by the general overview of the TFD methods from which one will be highlighted. It is the STFT method that is the cornerstone of the current thesis, used for vibration signal analysis. Therefore, a detailed mathematical background of the STFT will be discussed.

This will be followed by the introduction of the principal research flow. During this introduction, simulated signals will be presented, which will guide the descriptions through the next three chapters to demonstrate those different steps which ensure obtaining information from the transient signals.

In the last part of the chapter an algorithm will be proposed to improve the STFT spectrogram creation step.

2.1 Theoretical Basis

In this section the basics of the frequency domain transformations will be represented. The section will guide through on how TD signals can be transferred into FD using FT, DFT, FFT to represent spectral components followed by the summation of different spectra representations in various dimensions. Section 2.1 will be closed by the possible transient signal analysis methods and their comparison. This section is mainly the extraction of the content of references [7, 74–84, 84–88] found during literature research.

This section will discuss the basic FD analysis methods using references [7, 74, 76, 80, 82] as a basis, extended by the different spectra types [83]. [7, 83] was used a reference guideline for introduction of the STFT method.

2.1.1 Fourier Transform

The relationship between TD and FD is given by the Fourier series equation, which specifies that a signal can be written as the sum of sine and cosine functions. About these frequency elements, it can be said that their multiples are equal to the reciprocal of the original signal's period.

$$\mathrm{f}(t) = a_0 \sum_{k=0}^{\infty} (a_k \cos(\omega_k t) + b_k \sin(\omega_k t)) \tag{2.1}$$

where $\omega_k = k\omega_0 = k2\pi f_0 = 2k\frac{\pi}{T_0}$. The coefficients in Eq. 2.1 are

$$a_0 = \frac{1}{T_0} \int_{-T_0/2}^{T_0/2} \mathrm{f}(t) \mathrm{d}t, \tag{2.2}$$

$$a_k = \frac{2}{T_0} \int_{-T_0/2}^{T_0/2} \mathrm{f}(t) \cos(k\omega_0 t) \mathrm{d}t, \tag{2.3}$$

$$a_k = \frac{2}{T_0} \int_{-T_0/2}^{T_0/2} \mathrm{f}(t) \sin(k\omega_0 t) \mathrm{d}t. \tag{2.4}$$

The equation can also be written by combining the parts of the same frequency as

$$\mathrm{f}(t) = A_0 + \sum_{k=1}^{\infty} A_k \cos(\omega_k t + \varphi_k), \tag{2.5}$$

where

$$A_0 = a_0 \tag{2.6}$$

$$A_k = \frac{a_k}{\cos \varphi_k} = -\frac{b_k}{\sin \varphi_k} = \sqrt{a_k^2 + b_k^2} \tag{2.7}$$

$$\varphi_k = -\tan\left(\frac{a_k}{b_k}\right) \tag{2.8}$$

The f(t) periodic time function is represented by spectral lines described by A_k and φ_k values. The division between the spectral lines, i.e., the frequency resolution, can be calculated by the following formula

$$\Delta f = \frac{1}{T_0}. \tag{2.9}$$

It follows from Eq. 2.9 that the larger the time period (T_0) of the reference signal is, the closer the spectral lines are to each other.

The Fourier transform presented above is only suitable for converting deterministic signals. An algorithm that can also be applied to non-deterministic signals is obtained by transforming the periodic case equations. The T_0 period for deterministic signals can be approximated to infinity. In a discrete line spectrum, the Δf distance between the lines tends to zero due to the transformation and creates a continuous spectrum from the line spectrum. The sums in the formulae are replaced by the integral since the spectrum is obtained as the sum of infinitely small Δf values. The transformation is resulted into the general FT (Eq. 2.10) and the inverse FT (Eq. 2.11).

$$\mathrm{f}(t) = \int_{-\infty}^{+\infty} \bar{\mathrm{F}}(\omega) e^{j\omega t} \mathrm{d}f \tag{2.10}$$

$$\bar{\mathrm{F}}(\omega) = \int_{-\infty}^{+\infty} \mathrm{f}(t) e^{j\omega t} \mathrm{d}f \tag{2.11}$$

The presented FT, which can be applied in deterministic cases, cannot be easily handled by computers. Analogue signals must first be made processable, i.e., continuous signals must be sampled at discrete times. The value measured at each sampling point must be quantised and transmitted to the processing unit in a given form. The signals transformed in this way cannot be converted by the Fourier transform shown, so a particular version is used for this purpose. The algorithm is called DFT.

DFT generates a discrete frequency spectrum from the sampled discrete signals, which approximates the spectrum of the continuous signal generated by the FT. The DFT only provides an approximation because not all information about the continuous signal is available during the transformation since data loss occurs between two sampling times. If the sampling frequency is high enough, i.e., the time between two measurements is sufficiently short, the spectrum obtained with DFT is very close to the original.

The modified form of Eq. 2.11 is

$$\bar{\mathrm{F}}'(\omega) = \Delta t \sum_{n=-\infty}^{+\infty} \mathrm{f}(n\delta t) e^{j2\pi n f \Delta_t}. \tag{2.12}$$

$\bar{\mathrm{F}}'(\omega)$ is periodic based on ω therefore the spectrum is periodically repeated with $\frac{2\pi}{\Delta_t}$ frequency

$$\bar{\mathrm{F}}'(\omega) = \bar{\mathrm{F}}'\left(\omega + n\frac{2\pi}{\Delta_t}\right). \tag{2.13}$$

In the production of discrete signals, a prerequisite for correct sampling is to ensure that overlaps between identical components are avoided in the spectrum produced by the presented periodic repetitions. This means that only a band-limited signal can be examined with DFT, i.e. there is an upper-frequency limit determined by the sampling frequency (f_s) and time (Δ_t). According to the Shannon theorem, the highest testable frequency ($f_{\max}$) in the Fourier transform spectrum of the sampled signal is

$$f_{\max} \leq \frac{1}{2\Delta_t}. \tag{2.14}$$

Examining the analogue signal for a period of t_f, sampling at intervals of Δ_t, the number of sampling points is

$$N = \frac{t_f}{\Delta_t}. \tag{2.15}$$

The t_f is a characteristic value of time-limited signals, called observation time, or sampling window. This parameter profoundly affects the other sampling properties, as only a finite number of measurement points will be available for any sampling time. This also affects the value of the maximum frequency that can be analysed.

Taking t_f into account, the calculation of the following factors in the DFT formula changes as

$$\omega = N\Delta_\omega \qquad \text{or} \qquad f_s = N\Delta_m, \tag{2.16}$$

where

$$\Delta_\omega = \frac{2\pi}{t_f} = \frac{2\pi}{N\Delta_t}. \tag{2.17}$$

From N number of samples N number of spectral sample can be produced however only $\frac{N}{2}$ number of components will be independent of each other. As a result the spectrum contains relevant samples in the frequency range $0 ... \left(\frac{N}{2}-1\right) \cdot \Delta_\omega$. In section $\frac{N}{2} \cdot \Delta_\omega$ the imaginary part of the spectrum changes sign therefore this section contains redundant information.

The main relationships between Δ_t sampling time, $f_{\max}$ boundary frequency, Δ_f frequency resolution and N number of samples are

$$\Delta_t = \frac{1}{2 f_{\max}}, \tag{2.18}$$

$$f_{\max} = \frac{N \Delta_f}{2}, \tag{2.19}$$

$$\Delta_f = \frac{1}{N \Delta_t}. \tag{2.20}$$

The form of DFT described above is not directly applicable in practice, since even on modern computers, mapping the spectrum of simple signals would require so much computation that the operation would take an unacceptably long time. A very efficient computational method has been developed that significantly reduces this time, thereby accelerating the transformation. This is why it was called the Fast Fourier Transform.

FFT is an algorithm for calculating DFT that gives the same result with less computational effort. It breaks down a series of DFT values into frequency components, which is useful in many areas, but the process is very time consuming. For N samples, the DFT calculation would require a N^2 operation (multiplication and addition), while for a FFT, the $N \log_2(N)$ operation would be required to achieve the same result.

The speed difference can be huge, especially for long data streams, where N can be in the order of thousands or millions. In practice, the computation time can be reduced by orders of magnitude, and the rate of improvement is about equal to $\frac{N}{\log(N)}$. Because of FFT, it is worth using the DFT algorithm in different areas, such as digital signal processing or solving differential equations. However, there are limitations to using FFT, as the number of digital time signals must be two powers, and the frequency range of the analysis depends on the number of samples and the sampling rate. Despite its drawbacks, it is widespread and is now used by all spectrum analysis units.

When calculating FFT, the time and frequency information is not directly related to the algorithm, so the sampling time is needed to properly represent the data, from which the distance between the spectrum lines in Hz can be determined by Eq. 2.20. Applying the appropriate dimension and plotting the result, the spectrum of the analysed signal is obtained. There are multiple amplitude and phase dimensions to choose from, depending on the vibration components' characteristics under study. These possibilities are reviewed in the following subsections.

2.1.2 Spectrum Types

Before presenting the spectral types, it is required to note that the data generated by FFT from the vibration signal under study have two components, i.e., they have a real part and an imaginary part. Therefore, it is always necessary to switch to polar coordinates during the evaluation. The data generated by FFT will be represented by amplitude and phase values.

The most commonly used amplitude dimensions for plotting Amplitude Spectum (AS) are peak amplitude (V_{pk}) and effective amplitude (V_{RMS}).

The peak amplitude specifies the maximum amplitude of the vibration. Its typical application is the measurement of vibration displacement and the detection of needle pulses in vibration acceleration measurement.

The concept of effective or RMS amplitude is the same as the RMS value used in electronics. The RMS value of the alternating current is equal to the magnitude of the direct current that produces the same amount of heat at the same resistance in the same unit of time as the alternating current. The RMS value is thus proportional to the power of the signal. Commonly used when measuring vibration velocity and vibration acceleration. The relationship between RMS and peak amplitude is given by the following equation, which can also be used to generate spectral scales

$$V_{\mathrm{RMS}} = \frac{V_{\mathrm{pk}}}{\sqrt{2}}. \tag{2.21}$$

We can differentiate the spectra types according to which aspect and properties of the signal's frequency components they want to highlight. The first type analyses the essential factors of the components, i.e., their size and angle. These are called amplitude and phase spectra. The next large group includes the types that can be used to determine each frequency component's energy content based on its size. The variants belonging to this are called Power

Spectum (PS). In the last category are the types that represent the distribution, i.e., the density, of each component. Since no such spectrum can be generated for phase values, only amplitude and power spectral densities are included. Each type is closely related to each other, as in most cases, they have to be calculated from each other. Their visualisation depends on how we want to scale the magnitude of the frequency components: linear or logarithmic.

By default, the spectra take peak amplitude values and give a double-sided representation. The phenomenon is caused by the fact that the real signals are symmetrical around the signal with 0 Hz frequency, i.e. when mapping in the frequency range, a sample will have a positive and a negative value. From the test's point of view, the negative frequencies' information is redundant, irrelevant; therefore, the spectrum can be omitted when plotting. However, it must be taken into account that the energy content of the frequency components is evenly distributed between the negative and positive phase values. The equations required to produce single-sided spectral images can be found in Table 2.1.

By switching to simple polar coordinates and plotting the results by frequency, the amplitude and phase spectra are obtained. The equations of the transition can be found in Table 2.1.

Power values in the frequency components can be defined and represented by FFT or DFT by squaring the components' amplitude values. The power spectrum is by definition

$$\mathrm{S}_{xx}(f) = \mathrm{X}^*(f)\mathrm{X}(f) = |\mathrm{X}(f)^2|. \tag{2.22}$$

The equation for calculating the AS for discrete signals

$$\mathrm{S}_{xx}(i) = |\mathrm{X}_n(i)^2| = \left(\frac{\mathrm{X}_n(i)}{N}\right)^2. \tag{2.23}$$

Using the prescribed equation, the unit of power values for the phase components is the square of the peak amplitude (V_{pk}^2).

The power spectrum can also be given by the effective RMS amplitude values, which provide much more information about the signal. Here the transition takes place using Table 2.2. The equations prescribed for the single- and double-sided spectral representations are also valid in this case. When converting to RMS amplitude values, the unit of power for the frequency components is the RMS amplitude square (V_{RMS}^2).

Table 2.1: Summary of the dimensions and calculations of amplitude and phase spectra

Spectrum	**Scale**	**Equation**
Phase	rad	$\varphi i = \angle(X_N(i)) = \arctan\left(\frac{\mathrm{Im}X_N(i)}{\mathrm{Re}X_N(i)}\right)$
Amplitude	V_{pk}	$\mathrm{B}(i) = \begin{cases} X_N(0) & i = 0 \\ X_N(i) & i = 1, 2, ..., \lfloor \frac{N}{2} - 1 \rfloor \end{cases}$ $\mathrm{A}(i) = \lvert \mathrm{B}(i) \rvert = \sqrt{[\mathrm{Re}[\mathrm{B}(i)]]^2 + [\mathrm{Im}[\mathrm{B}(i)]]^2}$
	V_{RMS}	$\mathrm{C}(i) = \begin{cases} X_N(0) & i = 0 \\ \sqrt{2} X_N(i) & i = 1, 2, ..., \lfloor \frac{N}{2} - 1 \rfloor \end{cases}$ $\mathrm{A}(i) = \lvert \mathrm{C}(i) \rvert = \sqrt{[\mathrm{Re}[\mathrm{C}(i)]]^2 + [\mathrm{Im}[\mathrm{C}(i)]]^2}$
	dBV	$\mathrm{A}(i) = 20 \log_{10}(\mathrm{A}(i)[V_{\mathrm{pk}}, V_{\mathrm{RMS}}])$
	dBm	$\mathrm{A}(i) = 20 \log_{10}\left(\frac{\mathrm{A}(i)[V_{\mathrm{pk}}, V_{\mathrm{RMS}}]}{\sqrt{10^{-3}}}\right)$
Amplitude density	$\frac{V_{\mathrm{pk}}}{\sqrt{\mathrm{Hz}}}$	$\mathrm{B}(i) = \begin{cases} X_N(0) & i = 0 \\ 2 X_N(i) & i = 1, 2, ..., \lfloor \frac{N}{2} - 1 \rfloor \end{cases}$ $\mathrm{ASD}(i) = \frac{\mathrm{B}(i)}{\sqrt{\Delta_f \cdot \mathrm{ENBW}}} = \frac{\mathrm{B}(i)}{\sqrt{N \cdot \Delta t \cdot \mathrm{ENBW}}}$
	$\frac{V_{\mathrm{RMS}}}{\sqrt{\mathrm{Hz}}}$	$\mathrm{C}(i) = \begin{cases} X_N(0) & i = 0 \\ \sqrt{2} X_N(i) & i = 1, 2, ..., \lfloor \frac{N}{2} - 1 \rfloor \end{cases}$ $\mathrm{ASD}(i) = \frac{\mathrm{C}(i)}{\sqrt{\Delta_f \cdot \mathrm{ENBW}}} = \frac{\mathrm{C}(i)}{\sqrt{N \cdot \Delta t \cdot \mathrm{ENBW}}}$
	dBV	$\mathrm{ASD}(i) = 20 \log_{10}\left(ASD_0\left[\frac{V_{\mathrm{RMS}}}{\sqrt{\mathrm{Hz}}}, \frac{V_{\mathrm{pk}}}{\sqrt{\mathrm{Hz}}}\right]\right)$
	dBm	$\mathrm{ASD}(i) = 20 \log_{10}\left(\frac{ASD_0\left[\frac{V_{\mathrm{RMS}}}{\sqrt{\mathrm{Hz}}}, \frac{V_{\mathrm{pk}}}{\sqrt{\mathrm{Hz}}}\right]}{\sqrt{10^{-3}}}\right)$

The noise level of the measurement is closely related to the bandwidth of the measurement. When examining the basic noise level of a PS, all narrow-band noise levels in all FFT bands must be examined. Therefore, the noise level of a given spectrum depends on the value of Δ_f for the spectrum, which is determined by the sampling time and the number of sampling points in the measurement. In other words, the noise level at each frequency line is equal to the noise level that can be obtained by applying a Δ_f Hz filter around that frequency line. Therefore, by doubling the number of sampling data at a given sampling time, we can reduce the noise power, which appears in each frequency band. Theoretically, discrete frequency components have zero bandwidth and cannot be scaled by the number of points or the frequency range of the FFT.

In order to calculate the signal/noise relationship - Signal-to-Noise Ratio (SNR) - the power peaks for the frequencies under test have to be compared with the broadband noise level. The broadband noise level is calculated by summing all power spectra in a band except the peaks and the zero-frequency component and then dividing the sum by the equivalent noise width of the window.

The Power Spectral Density (PSD) normalises the spectrum compared to a spectrum provided by an ideal, generally accepted 1 Hz filter for measuring noise levels. Each frequency line level is the same as that which would be obtained if the 1 Hz filter were applied around a given frequency line. Another spectrum can be derived from the power spectrum density called Amplitude Spectral Density (ASD). The equations needed to determine the two types of spectra are shown in Table 2.2.

From the definition of the power and amplitude spectrum densities, the spectral characteristics of the measured signal are improved utilising filters (windows). The essence of the method is that when performing Fourier or spectral analysis, windows can minimise the truncated waveforms' interruptions, and the scattering of the spectrum is reduced. The filter reduces the amplitude of interruptions and thus behaves like a narrow-band low pass filter. In the windowing process, the given finite length window is multiplied by the measured signal of finite length. So we have to use filters in our tests, many types of which are known.

An FFT is equivalent to using a series of parallel filters, where the bandwidth of each filter is equal to $\Delta\Phi$. Due to the spreading effect of the smoothing window, the smoothing window increases the effective bandwidth of the FFT band by a value called Equivalent Noise-power Bandwidth (ENBW). The peak energy of a given frequency is equal to the sum

Table 2.2: Summary of the dimensions and calculations of power spectra

Spectrum	Scale	Equation
Power	V_{pk}^2	$\text{B}(i) = \begin{cases} X_N(0) & i = 0 \\ 2X_N(i) & i = 1, 2, ..., \lfloor \frac{N}{2} - 1 \rfloor \end{cases}$ $\text{S}_{xx}(i) = \lvert \text{B}(i) \rvert^2$
	V_{RMS}^2	$\text{C}(i) = \begin{cases} X_N(0) & i = 0 \\ \sqrt{2}X_N(i) & i = 1, 2, ..., \lfloor \frac{N}{2} - 1 \rfloor \end{cases}$ $\text{S}_{xx}(i) = \lvert \text{C}(i) \rvert^2$
	dBV	$\text{S}_{xx}(i) = 10 \log_{10}(\text{S}_{xx}(i)[V_{\text{pk}}, V_{\text{RMS}}])$
	dBm	$\text{S}_{xx}(i) = 10 \log_{10} \left(\frac{\text{S}_{xx}(i)[V_{\text{pk}}, V_{\text{RMS}}]}{\sqrt{10^{-3}}} \right)$
Power density	$\frac{V_{pk}^2}{Hz}$	$\text{B}(i) = \begin{cases} X_N(0) & i = 0 \\ \sqrt{2}X_N(i) & i = 1, 2, ..., \lfloor \frac{N}{2} - 1 \rfloor \end{cases}$ $\text{PSD}(i) = \frac{\lvert \text{B}(i) \rvert^2}{\Delta f \cdot \text{ENBW}} = \frac{\lvert \text{B}(i) \rvert^2}{N \cdot \Delta t \cdot \text{ENBW}}$
	$\frac{V_{\text{RMS}}^2}{Hz}$	$\text{C}(i) = \begin{cases} X_N(0) & i = 0 \\ \sqrt{2}X_N(i) & i = 1, 2, ..., \lfloor \frac{N}{2} - 1 \rfloor \end{cases}$ $\text{PSD}(i) = \frac{\lvert \text{C}(i) \rvert^2}{\Delta f \cdot \text{ENBW}} = \frac{\lvert \text{C}(i) \rvert^2}{N \cdot \Delta t \cdot \text{ENBW}}$
	dBV	$\text{PSD}(i) = 10 \log_{10} \left(PSD_0 \left[\frac{V_{\text{RMS}}}{\sqrt{\text{Hz}}}, \frac{V_{\text{pk}}}{\sqrt{\text{Hz}}} \right] \right)$
	dBm	$\text{PSD}(i) = 10 \log_{10} \left(\frac{PSD_0 \left[\frac{V_{\text{RMS}}}{\sqrt{\text{Hz}}}, \frac{V_{\text{pk}}}{\sqrt{\text{Hz}}} \right]}{10^{-3}} \right)$

of the frequency bands adjacent to the peak, increased by a proportionality factor equal to the ENBW of the smoothing window. The proportionality factor should be taken into account when performing a calculation based on the power spectrum.

The types of applicable windows and their mathematical details can be found in [74]. The more-in-depth mathematical introduction of the filtering windows is outside of the scope of the thesis.

2.1.3 Time-Frequency Domain Analysis for Transient Signal Evaluation

The FD represents the signal's spectral components, and the time distribution information of the spectral components is often included in the phase characteristic of the FT. However, it is not easy to use this information about the time distribution in the frequency domain. Besides, the basic assumption when we transform a signal to its frequency domain is that its frequency components do not change over time, i.e., the signal is stationary. Thus, the FT in the frequency domain cannot provide a time distribution information of the spectral components. Most analysis of rotating machines is based on examining the vibrations during a speed sweep, where machines are either accelerated up from low to high RPM or slowed down from high to low RPM. This often results in non-stationary signals whose frequency content changes over time [7].

The time-frequency domain has been used for non-stationary, transient waveform signals. Therefore several time-frequency analysis techniques have been developed and applied to machinery condition monitoring: e.g. STFT, WT, HHT which are represented in [7].

The STFT is the first modified version of the FT that allows one to analyse non-stationary signals in the time-frequency domain. The basic idea of the STFT is that instead of computing the DFT of the whole signal, the signal is decomposed into shorter segments of equal length using a time-localised window function. After this, perform the DFT separately on each windowed segment of the signal, which together forms the time-frequency spectrum of the signal [7].

Wavelet analysis is another time-frequency domain analysis approach that decomposes the signal based on a family of 'wavelets'. The way wavelet analysis localizes the signal's information in the time-frequency domain through variable spectrograms makes it an attractive alternative analysis method to the STFT method for the analysis of non-stationary signals. Unlike the window used with the STFT, the wavelet families have fixed shapes – e.g. Haar, Daubechies, Morlets etc. – but the wavelet function is scalable, which means the WT is adaptable to a wide range of frequency- and time-based resolutions [7]. The mother wavelet $\psi(t)$ can be expressed mathematically by the following equation

$$\psi_{s,T}(t) = \frac{1}{\sqrt{s}}\psi\left(\frac{t-T}{s}\right), \tag{2.24}$$

where s represents the scaling parameter, T is the transformation parameter, and t is the time. The original mother wavelet has $s = 1$ and $T = 0$. The three main transforms in wavelet analysis are the Continous Wavelet Transform (CWT), Discrete Wavelet Transform (DWT) and Wavelet Packet Transform (WPT) [89]. More details of the similarities and the differences between the STFT and WT can be read in [90].

More methods and a more in-depth description of the TFD methods themselves can be found in Part II, Chapter 5 of [7]. The other fundamental part of this research is STFT analysis, thus in accordance with this, more mathematical details about the STFT can be found in this thesis in section 2.2.

2.2 Short-Time Fourier Transform

The mathematical background of STFT will be presented at this part which is the basis of the thesis. The resulted in spectrogram is the common starting point of every further step introduced in the following main and subsections. This section is mainly the extraction of the content of references [83, 91–93] found during literature research because the STFT is commonly used method for transient signal analysis.

Generally, not only stationary signals have to be analysed in frequency domain. The main problem in the case of transient signals is that the FT can not represent the signal's time-variant behaviour. The STFT is a function based on DFT that determines the sinusoidal frequency and phase components of specific sections of a time-dependent continuous signal. In practice, in the production of STFT, a longer time signal is split into several smaller segments of equal length, on which the discrete Fourier transform is performed one by one. The result gives the frequency spectrum of each section. The results are plotted against time to obtain the time-dependent frequency spectrum, i.e., the spectrogram. The FFT is an excellent mechanism for finding the frequency components of a signal, but its result does not depend on the time course. The essence and significant advantage of the STFT method lies in the fact that it can analyse the time and frequency dependence of a signal at the same time.

In order to introduce the mathematical basis of STFT, we have to start by giving us a finite, complex, univariate, discrete-time series of length M, i.e., the time signal points are

$$\{X_t\}_{t=0}^{M-1}. \tag{2.25}$$

The DFT of the input signal can be calculated as

$$D_k = \frac{1}{\sqrt{M}} \sum_{j=0}^{M-1} X_j \omega_M^{-jk}, \tag{2.26}$$

where $K = 0, 1, ...M - 1$ and

$$\omega_M^{-jk} = \exp\left(\frac{i2\pi l}{M}\right) = \cos\left(\frac{2\pi l}{M}\right) + i \sin\left(\frac{2\pi l}{M}\right). \tag{2.27}$$

The DFT is basically the same as a least-squares regression applied to signals of different frequencies in the period $\frac{M}{2}$. The method can be used to find the coefficients for the amplitude and phase values at which the residual errors are zero. The original signal can be reconstructed using inverse DFT using the coefficients of the DFT.

In order to ensure that the transformations described above exist, the input signal has to meet the following condition

$$D_k = \frac{1}{\sqrt{M}} \sum_{j=0}^{M-1} |X_j| < \infty. \tag{2.28}$$

The STFT can be generated by a DFT applied to a continuous section extracted from the input signal, where the number of data points is $N < M$. This interval is called the window. First the value of $(X_0...X_{M-1})$ of the DFT has to be determined. In the next step, the window has to move by one time index and perform the DFT transformation again on the new interval $(X_1...X_N)$. This step is repeated until the windowing procedure covers the last N data points from the input signal and the DFT transformation is performed here on the range $(X_{MN}...X_{M-1})$. The calculation of the DFT by definition is

$$\mathbf{A}_k^t = \frac{1}{\sqrt{N}} \sum_{j=0}^{N-1} X_{j+t-N+1} \omega_N^{-jk}. \tag{2.29}$$

During the generation of STFT, each data point X_j will be taken into account N times in the DFT calculations. Due to overlapping windowing, the result of STFT is affected by the time dependence of the input signal. It is noted that in case $N = M$ the STFT resulted in the same as it is given by DFT. In the case of $N = M$, of course, STFT is the same as DFT calculated for the entire data set. The result of Eq. 2.29 is $\mathbf{A}_k^t$ which is a complex valued matrix $\mathbb{C}^{N \times M-N+1}$ The result can therefore be considered as a series of time functions of complex value of N, which are $(M - N + 1)$ long.

It is noted that t denotes the time dependence of the matrix in its horizontal direction, while k denotes the frequency dependence vertically.

The calculation method presented above is very time-consuming due to the already known disadvantage of calculating DFT. Therefore, this time should be reduced to improve usability. Suppose, in the methods described above, the windows move with only one time index. In that case, two window positions in the given region can be taken into account and used in the calculation, thus reducing its time requirement. The relationship between the DFTs calculated for the two windows is given by the following equation

$$\mathbf{A}_k^{t+1} = \omega_N^k \left(\mathbf{A}_k^t - \frac{1}{\sqrt{N}} X_{t-N+1} + \frac{1}{\sqrt{N}} X_{t+1} \right). \tag{2.30}$$

The formula can also be written in the following form if the window moves more than one step $(s \geq 1)$

$$\mathbf{A}_k^{t+s} = \omega_N^{ks} \left(\mathbf{A}_k^t + \frac{1}{\sqrt{N}} \sum_{j=0}^{s-1} (X_{t+1+j} - X_{t-N+1+j}) \omega_N^{-jk} \right). \tag{2.31}$$

Once the first matrix $\mathbf{A}_k^t$ was calculated, i.e., the DFT result of $X_{t-N+1}...X_t$, this can be used in the following steps during the DFT calculation of $\mathbf{A}_k^{t+s}$, i.e., during the DFT calculation of $(X_{t+s-N+1}...X_{t+s})$. In the case of $s \geq N$, then the two DFT calculations are independent from each other which means this is not STFT, but a batch of DFT calculations, and the time required for the calculation is not reduced. The formula takes advantage of the computational redundancy due to overlapping windows, which reduces the calculation time.

Dénes Gábor used first the STFT calculation for the analysis of speech data in 1946. Due to this, STFT is mentioned in the literature in several different forms, such as the windowed FT, the Gábor-transformation, or the local FT. The form of STFT used in this dissertation is a special case of the Gábor-transformation. In the latter case, each of the inputs delimited by each window is weighted by coefficients of different magnitudes c_j. The method's essence is to highlight as many values in the middle of the window as possible, and the ones at the edge of the window should play a smaller role. The Gábor-transformation can be described as

$$\mathbf{A}_k^t = \frac{1}{\sqrt{N}} \sum_{j=0}^{N-1} (c_j X_{j+t-N+1}) \omega_N^{-jk}. \tag{2.32}$$

The above-mentioned equation is a much more general form of the STFT calculation, which can easily be transferred into the same form introduced before, if $c_j = 1$ for every j.

In the above, one interpretation of the STFT calculation was presented that focused on showing the close relationship with DFT. In the following, another approach is described, which focuses more on making the result of the FT time-dependent, i.e., using windows.

The primary problem is that the FT does not represent the time-dependent behaviour. In order to address the deficiency, a simple method can be used in which the signal is compared with elementary functions that are simultaneously localised in a time and frequency domain. The equation that mathematically describes the method is shown below as

$$\mathrm{STFT}(t, \omega) = \int \mathrm{x}(\tau) \gamma_{t,\omega}^*(\tau) \mathrm{d}\tau = \int \mathrm{x}(\tau) \gamma^*(\tau - t) e^{-j\omega\tau} \mathrm{d}\tau, \tag{2.33}$$

where $\gamma^*(\tau)$, called window function, usually has a short duration compared to the input signal $\mathrm{x}(t)$. For this reason, the calculation STFT is also called a windowed Fourier transform. An approach to the calculation process of the formula is shown in Fig. 2.1 and an illustration of a resultant spectrogram can be seen in Fig. 2.2.

As a first step, the input signal is multiplied by $\mathrm{x}(t)$ and the window function $\gamma^*(\tau)$, and the result $\mathrm{x}(\tau)\gamma^*(\tau - t)$ has to be Fourier transformed. The window function is valid only for a small period of time, so the result of the FT only reflects the local frequency properties of the signal. By moving the window function and repeating the calculation process, we can get an idea of how the frequency components of the input signal change with time. The result of the FT will thus be a complex valued function representing the time- and frequency-dependent phase and amplitude characteristics of the input signal.

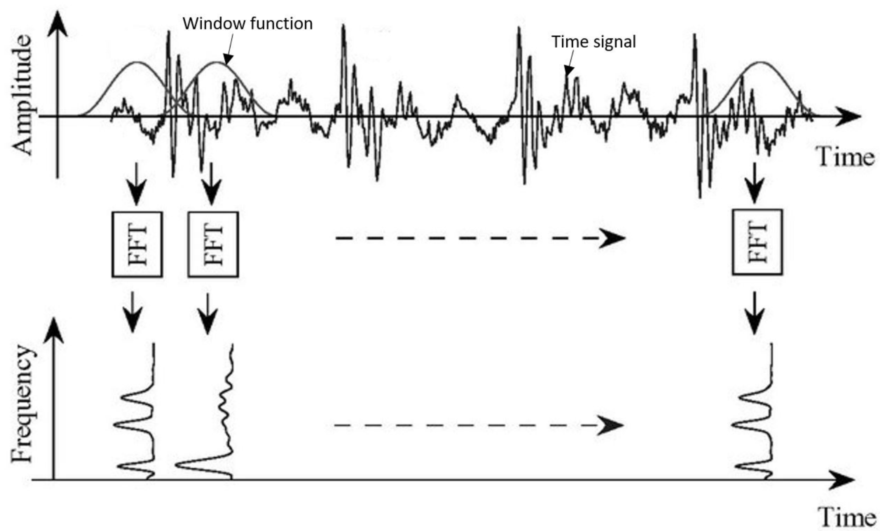

Figure 2.1: Illustration of the Short-Time Fourier Transform (STFT) [81]

Let us assume that the window function at time instance $\mathrm{x}(\tau)\gamma^{*}t = 0$, while its FT for $\omega = 0$ frequency component is symmetric. If the duration and frequency bandwidth of $\mathrm{x}(\tau)\gamma^{*}$ are Δt and $\Delta\omega$, then the $\mathrm{STFT}(t,\omega)$ will represent the behaviour of the signal in the neighbourhood of the $[t-\Delta_t, t+\Delta_t] \times [\omega-\Delta_\omega, \omega+\Delta_\omega]$ range.

In order to be able to measure a signal as accurately as possible in a specific time and frequency range, Δt and $\Delta\omega$ limits should be chosen as narrow as possible. However, it contradicts the requirement that the two coefficients are related to each other through the FT. The problems with the resolutions will be discussed in the next chapter.

By squaring and plotting the result of STFT, the STFT spectrogram (Eq. 2.34) can be obtained, which makes it easy to distinguish the diagram from other time-dependent spectra based on linear techniques. It is the most straightforward and most widely used time-dependent spectrum representing a signal's energy distribution over a time-frequency range. While the result of the STFT calculation is usually complex, the STFT spectrogram is typically real.

$$\mathrm{Spectrogram}(t,\omega) = |\mathrm{STFT}(t,\omega)|^2 \tag{2.34}$$

In the case of the STFT of discrete-time input signals, the relationships that are already known can be applied. Using a sample-based windowing technique, the data is split into equal-sized pieces that overlap each other—the larger the overlap, the smaller the changing

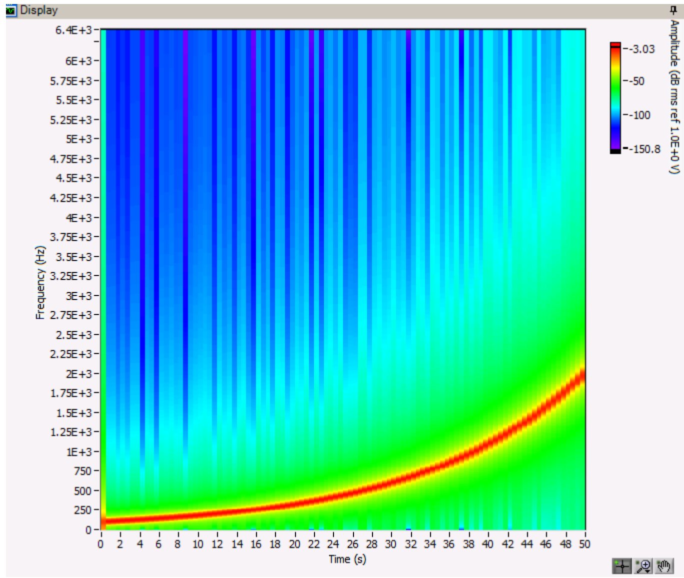

Figure 2.2: Illustration of a spectrogram (`www.ni.com`)

effect between them. A FT is performed on each data segment, the complex results are added to a matrix that captures the time- and frequency-dependent phase and amplitude properties for each point. The mathematical form of the method is

$$\mathrm{STFT}[k,n] = \sum_{i=0}^{L-1} \mathrm{x}[i]\gamma[i-k]W_L^{-ni}, \tag{2.35}$$

where

$$\mathrm{STFT}[k,n] = \mathrm{STFT}(t,\omega)|_t = kD_t, \tag{2.36}$$

and where

$$\omega = \frac{2\pi n}{LD_t} \tag{2.37}$$

Therefore the result after substitution is

$$\mathrm{STFT}\left\{\mathrm{x}[n]\right\}(m,\omega) = \sum_{n=-\infty}^{\infty} \mathrm{x}[n]\mathrm{w}[n-m]e^{-j\omega n}, \tag{2.38}$$

where $\mathrm{x}[n]$ is the time signal to be transferred, $\mathrm{w}[n-m]$ is the window function with a smaller duration related to the input signal and j is the complex unit.

The magnitude squared of $\mathrm{STFT}\left\{\mathrm{x}[n]\right\}(m,\omega)$ yields the visual representation of the transformation - the spectrogram itself in this case also using

$$\text{Spectrogram}\left\{\mathrm{x}[n]\right\}(m,\omega) = \left|\text{STFT}\left\{\mathrm{x}[n]\right\}(m,\omega)\right|^2 \tag{2.39}$$

Any of the previously introduced spectra types in section 2.1.2 can be used for spectrogram creation. In this research the basis of the spectrogram is always the PSD with the dimension of $\frac{\mathrm{V}_{\mathrm{pk}}^2}{\mathrm{Hz}}$.

2.2.1 Windowing Criteria and Resolution Issues

During this section, the windowing effect and the time versus frequency resolution optimum will be discussed. This discussion will involve the basis for eliminating this effect better to ensure high-quality spectrogram generation. The theoretical basis of this section is based on references [83, 92].

The most important disadvantage of the STFT is that it has fixed resolution in time and frequency influenced by the windowing process. The reason is that it determines whether the frequency resolution is appropriate, i.e., those frequency components which are close to each other can be distinguished from each other; or the time resolution is acceptable, so at certain times frequency changes can be separated.

The window size applied to the input signal determines the final frequency resolution. This could lead to better detachment of the frequency components, which are close to each other. The other circumstance is when the time-resolution is improved. In this case, the time instants at frequency changes become separable. A wide window creates ideal frequency resolution and disadvantageous time resolution, while a narrow window has a contrary effect. These effects are called narrow- and broadband resolution. The differences between these effects are shown in Fig. 2.3. The figure shows the fundamental difference between narrow-band (left) and broad-band (right) windows in terms of time and frequency resolutions. Therefore, when choosing the two parameters, it is crucial which property needs to be in focus in the end result.

However, the optimum between them can be taken into account when determining the resolutions. Consider the zero-center window functions, i.e., where time resolution is dependent on $\gamma^*(\tau)$, while its Fourier transform is symmetric for frequency components $\omega = 0$. In this case, the bandwidth of the two ranges is equal to the normal distribution of the variables, i.e., Δt for time and $\Delta\omega$ for frequency (the range is: $[t-\Delta_t, t+\Delta_t] \times [\omega-\Delta_\omega, \omega+\Delta_\omega]$.

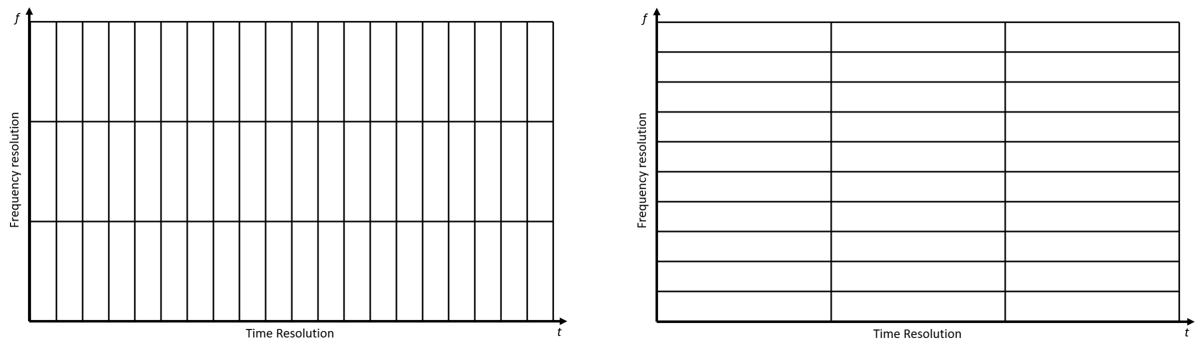

(a) Narrow window (b) Wide window

Figure 2.3: Wide and narrow window types

To reach the optimum, the two parameters must correspond to the so-called uncertainty inequality, which is as

$$\Delta_t \Delta_\omega \geq \frac{1}{2}. \tag{2.40}$$

The limit of inequality, i.e., the optimum of time and frequency resolution, can be achieved using Gaussian windows. This is because the zero-centricity of these functions is the most ideal in both time and frequency domains. Therefore, this window is most often used in various applications of STFT, but Hanning, Hamming, and triangle functions are also used [74, 94], as their properties are also favourable.

Resolution problems can be examined as a function of sampling- and Nyquist-frequency. Consider a window of N samples extracted from an arbitrary signal of real value, sampled at a frequency of f_s. As a result of the FT, N complex pairs of values are created on the image. Since we are talking about a real-valued signal, only half of the result can be considered useful, since its last half ($\frac{N}{2}$ points) is the complex conjugate pair in the reverse order of the first half. The coefficient $\frac{N}{2}$ thus represents the Nyquist-frequency ($\frac{f_s}{2}$) and the distance between each point is $\frac{f_s}{N}$ Hz.

This distance should be reduced to increase the frequency resolution. There is the possibility of reducing the f_s sampling frequency, without influencing the number of N points in the window. As described, the window size will increase as fewer sampling points will be available per time unit. The other option is to increase the number of N points in the window without changing the f_s sampling frequency. In this case, we get the same result. Thus, it can be seen that whichever path is chosen to increase the frequency resolution; it

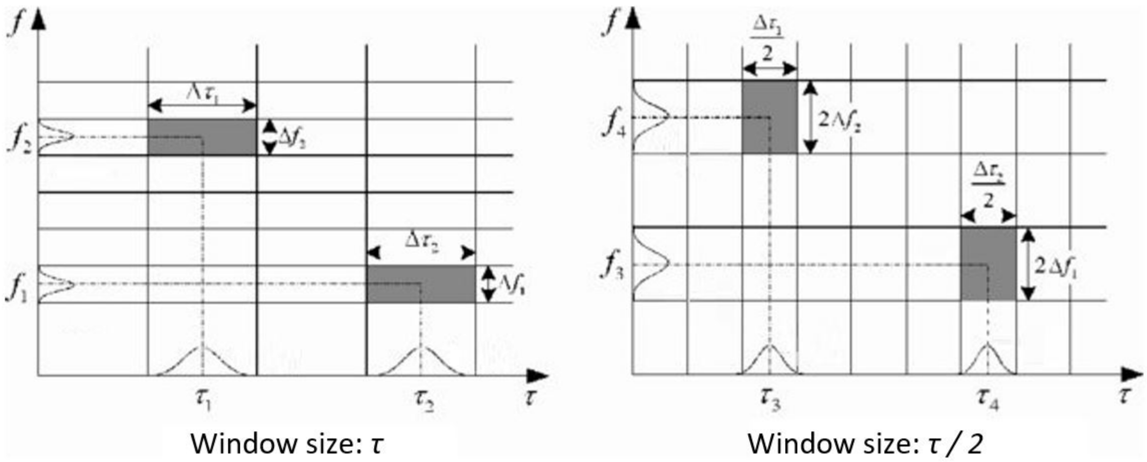

Figure 2.4: Illustration of the Time-frequency resolution during STFT [81]

generates a larger window that decreases the time resolution. The phenomenon also applies backwards, i.e., changing the two parameters in opposite directions has a similar effect on resolving the time and frequency ranges.

The Nyquist-frequency determines the maximum frequency that can still be processed for a given signal. The Rayleigh-frequency gives the minimum frequency that can still be processed by a finite time window for the same signal [95]. Suppose the width of the time window is t_{W} seconds, at which the minimum resolvable frequency is $\frac{1}{t_W}$ Hz. It is very important to determine this parameter in some applications, as valuable information can be lost during the study (e.g., neural signals).

Another condition is also necessary during the windowing procedure. The process itself can be determined in a way that the analysed time signal and, consequently, window functions will have some overlapping with each other. This means the STFT calculation of the given time window will be influenced by the time window in the previous step. The more overlapping between the used window is, the lower the switching effect between each section is. To get the most informative results from a signal, it is necessary, besides the time signal's high sampling frequency, to optimise STFT time and frequency resolution. Because in a construction, several rotating elements can be found, we decided to achieve high-frequency resolution in a time segment for spectrogram creation with the application of an overlapping windowing technique. During the analysis, it was assumed that the time segments are narrow enough to be considered quasi-stationary segments. The calculation of the spectrogram in the first analyses was time-consuming.

The best results can be achieved with big window overlapping while the data will be processed redundant, and the number of points used for FFT calculation can also be increased. Obviously, the complete algorithm has an upper limit related to the number of points and the overlapping ratio resulting in memory allocation issues. Using the improved memory management presented in the next sections, this phenomenon did not occur during the research work.

After a specific limit, the STFT algorithm ran into an error due to a lack of memory at the set values. At this moment, it has to be noted that the signal processing software package was developed using a 32-bit NI LabVIEW 2014 programming environment. It turned out that the cycles used in the algorithm could not store as much data as would have been needed. As a workaround for this problem, an enhanced Functional Global Variable (FGV) was used which is an often-used design pattern. An FGV is basically a non-reentrant function featuring a while loop that iterates once, and has an un-initialized shift register.

The essence of FGV is that the input data is stored globally in memory, from which it can then be retrieved later. The basis memory management was improved, which means dedicated memory segments were allocated to perform the FFT. Thanks to this, several FFT calculation can be performed parallel and using the proper indexing, the reconstruction of the STFT can be achieved. This can be performed because theoretically, the windowing is not else than cutting a section from the original time signal and performing the analysis on this time signal. When the complete signal is transformed, the results will be collected from the assigned memory addresses to display the spectrogram image for post-processing purposes.

Using the above mentioned techniques it possible to implement a subroutine capable of producing a more stable, reliable, and optimal result than its counterpart found in LabVIEW, which greatly facilitated subsequent studies. The block diagram of the solution can be seen in Fig. 2.5

2.3 Simulated Signals for Method Introduction

In the following sections and chapters of the thesis, a novel, multi-discipline evaluation method will be presented, which is visualised with a flowchart in Fig. 2.6.

The process was separated into three main phases. The thesis is structured in such a way

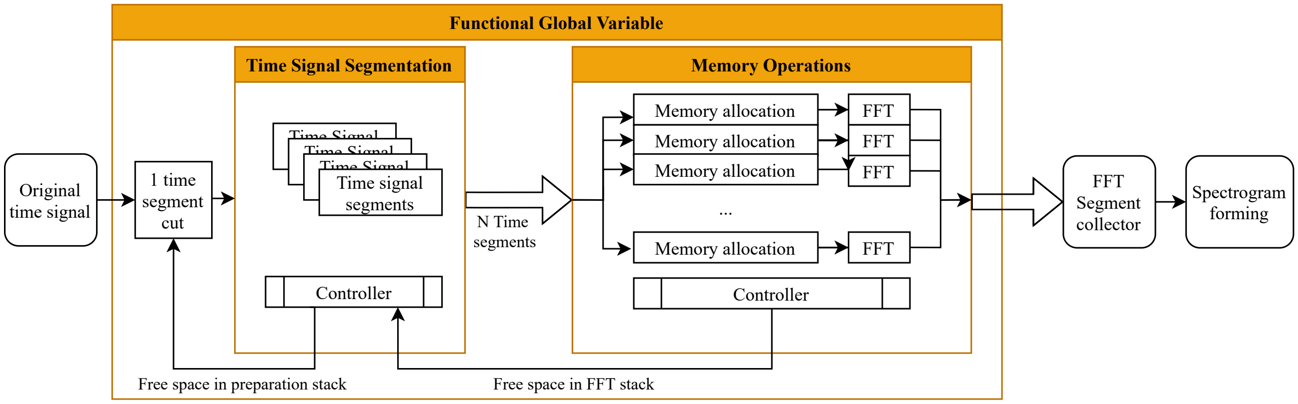

Figure 2.5: The block diagram of the improved STFT algorithm

that these main process phases are discussed during the chapters. The first part is a sequence of general vibration signal preparation and evaluation methods, which was discussed in this Chapter 2. This is follow by the second part of the process where the evaluation of the spectrogram image derived from the pre-processed signals takes place (Chapter 3 and first half of Chapter 4). The final phase is a transformation back into the Time-Freuqency (TF) domain (presented at the end of Chapter 4) to describe the operational state and create a basis for further diagnostics of the rotating machine about which Chapter 5 will represent more details.

In this chapter, simulated vibration signals were used for demonstration and validation purposes with 52 kS/s sampling. The sampling rate is in accordance with the bandwidth of the knock sensor used later in real measurements. The signals contain the superposition of multiple sine waves with defined amplitudes and frequencies, including noise. In order to check and validate the operation of the method, the simulated signals were extended with various noise signal conditions in addition to having different RPM gradients. The noise conditions were interpreted with the SNR and Total Harmonic Distortion (THD) values. During the analysis, SNR was determined by calculating the ratio of the fundamental tone RMS level and the noise RMS. In the simulations, an additional goal was to identify the lowest SNR, enabling the method to remain operational. The RPM gradients were defined by using practical applications; e.g. acceleration of an electric vehicle or acceleration of a car equipped with ICE during the 1st gear. Details about the simulated signals used for method verification are presented in Table 2.3 and 2.4. Table 2.3 contains those setups where the RPM gradient is changed, and the SNR without harmonics is 5 dB. Table 2.4 contains those setups

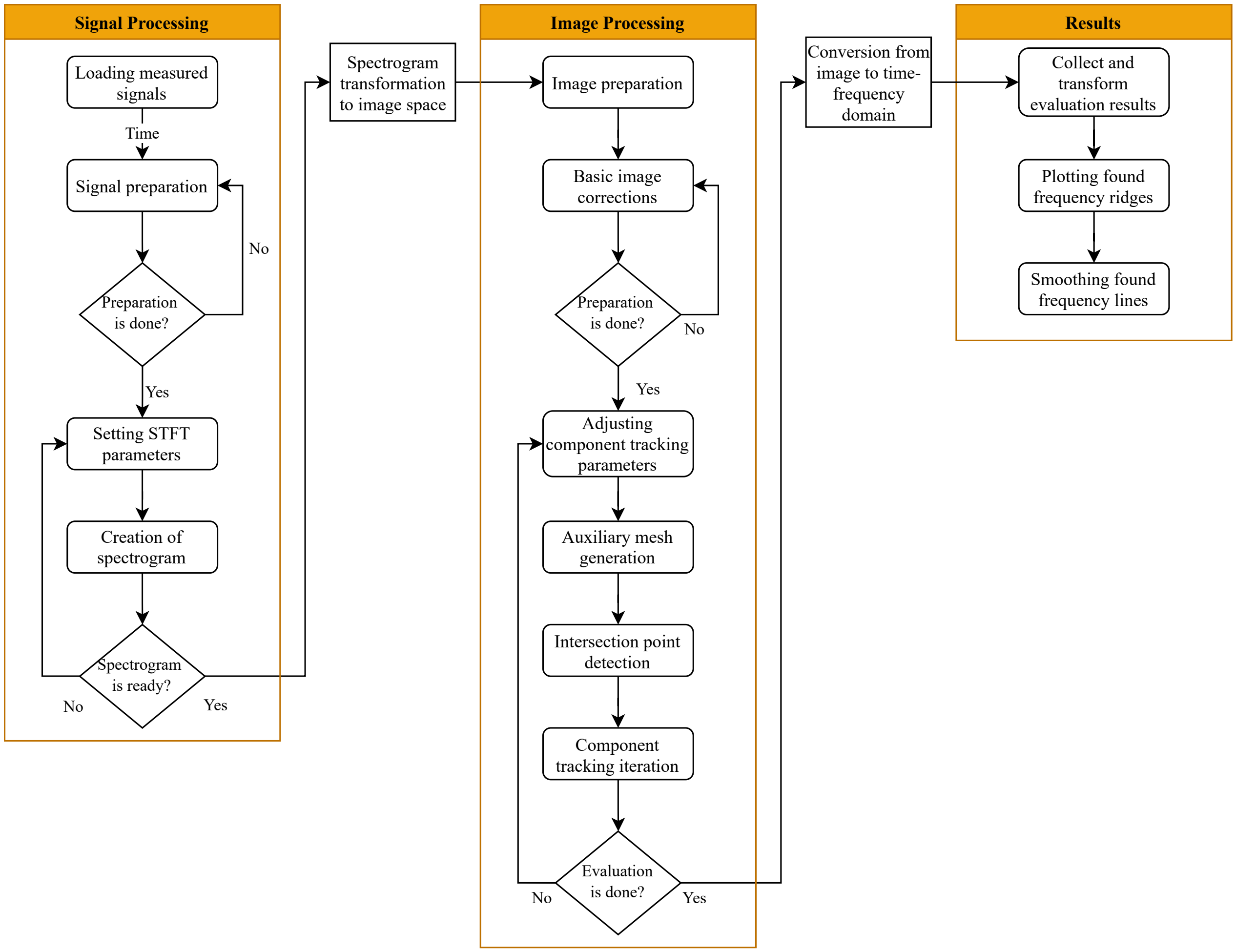

Figure 2.6: The flowchart of the developed method using improved STFT algorithm and image evaluation

where SNR is varied, and the gradient is fixed with a value of 3000 RPM for 1 second. The noise content was generated using Gaussian and Uniform White noise signals. The simulated signal generation was performed by the superposition of different, pre-generated waveforms. The signals consist of principal unit sine waves and different type of noise waveforms. The general description of one signal is

$$\mathrm{f}(t) = \sum_{1}^{N}(\sin(\omega_1 t) + ... + (\sin(\omega_N))) + \mathrm{G}^*(t) + \mathrm{U}^*(t), \tag{2.41}$$

where N is the number of the unit sine waves in the signal, ω_N is the frequency of one sine wave, $\mathrm{G}^*(t)$ is the Gaussian White Noise (GWN) time function and $\mathrm{U}^*(t)$ is the Uniform White Noise (UWN) time function.

Besides, for simulated signal generation, a gradient can be defined, which ensures different RPM gradient change in the signal in order to simulate different rotating frequency changes. The basis of the gradient is the ω_N value of the unit sine wave, which multiplied or divided by an integer will result in the start (f_{start}) and the end (f_{end}) frequencies.

Table 2.3: Main properties with transient info of the simulated signals used for validation

Setup	**Signal properties**	**Transient info**
1 - Ramp down	Unit amplitude sine waves $f_{\text{start}} = 1250; 3750; 8750$ and 12500 Hz	length = 2 s $f_{\text{end}} = \frac{f_{\text{start}}}{5}$
2 - Ramp up	Unit amplitude sine waves $f_{\text{start}} = 250; 750; 1750$ and 2500 Hz	length = 2 s $f_{\text{end}} = 5f_{\text{start}}$
3 - Ramp up	Unit amplitude sine waves $f_{\text{start}} = 50; 150; 500$ and 1750 Hz	length = 1 s $f_{\text{end}} = 5f_{\text{start}}$
4 - Ramp down	Unit amplitude sine waves $f_{\text{start}} = 150; 450; 1500$ and 5250 Hz	length = 0.5 s $f_{\text{end}} = \frac{f_{\text{start}}}{3}$

Table 2.4: Main properties with noise conditions of the simulated signals used for validation

Setup	**Signal properties**	**Noise info**
5 - Ramp up	Unit amplitude sine waves $f_{\text{start}} = 150$ and 500	SNR = -22.9 dB THD = 6.7 dB
6 - Ramp up	Unit amplitude sine waves $f_{\text{start}} = 150$ and 500	SNR = -19.1 dB THD = 1.99 dB
7 - Ramp up	Unit amplitude sine waves $f_{\text{start}} = 150$ and 500	SNR = -15.9 dB THD = -2.37 dB

The best results can be achieved with large window overlapping while the data will be processed redundant, and the number of points used for FFT calculation can also be enhanced. The overlapping conditions are influencing the smoothness of the final results. When the overlapping factor increases, the computational resource needs will be higher, but the results will have fewer errors. The influence of the overlapping phenomenon can be an area for further improvement. The actual recommendation for the overlapping is a constant 1/5 factor, i.e., 1/5 of a time segment will be used redundantly during every STFT operation step while the frequency resolution - the frequency bin parameter - needs to be close to half of the sampling frequency. The bin parameter can be determined by the ratio of the sampling frequency and the length of the FFT. During the validation, the time window is always 0.05 s wide with a 0.01 s overlapping, and the frequency bin parameter is 26 k. As an example, a simulated time signal and a generated spectrogram can be seen in Fig. 2.7.

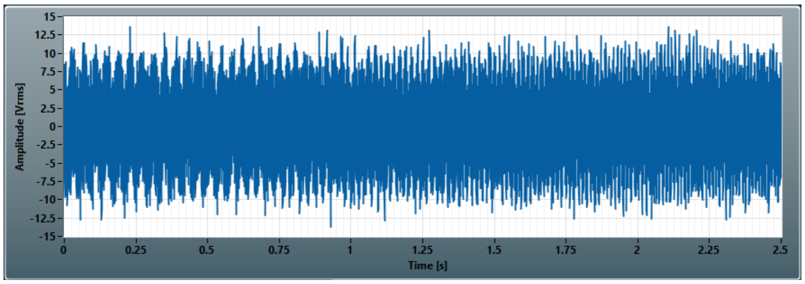

(a) The simulated time signal

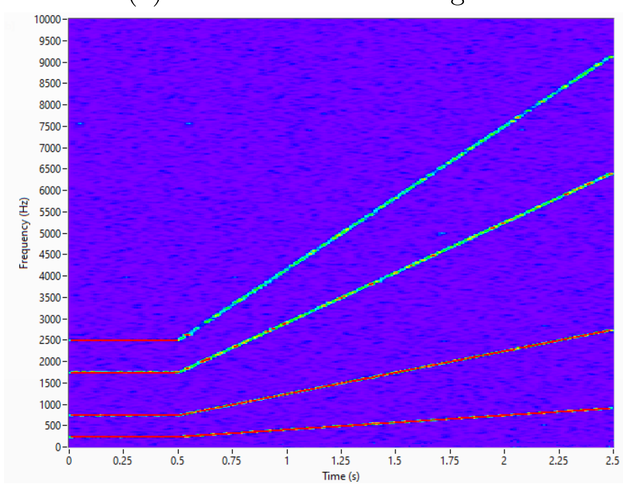

(b) The generated spectrogram

Figure 2.7: Time signal and spectrogram of Simulation Setup 2 in Table 2.3. The colour of the spectrogram indicates the amplitude values of the vibration components

2.4 Novel results

In this section those novel results will be summarized which are related to the part of the research work presented in Chapter 2.

2.4.1 Thesis 1

Algorithm enhancement for Short-Time Fourier Transform

The applied window function facilitates the enhancement of the Short-Time Fourier Transform process of a rotating machine vibration signal by parallelization of the calculation. The parallelization requires the definition of a batch of time segments for Fast Fourier Transform, dedicating a single processor core and allocating dedicated memory areas to parallelly process the defined time segment.

Related publications: [MG1]

Chapter 3

Spectrogram Image Processing

The main part of the research was to find out how to extract information from spectrograms fast and reliable without losing any information. The spectrogram can correspond to a map where the third dimension is represented with colours or colour-densities, we can correlate it to a Moiré-image. The difference in this aspect is that the black "Moiré" lines represent the exact frequency component trends which will be the basis of the next steps. Several research work represents Moiré-image evaluations in [96–100] and references [101–105] were also used during the creation of Chapter 3.

3.1 Vibration to Image Space

The first step is to transfer the information from vibration to Image space in order to extract information later. This can be performed by exporting the spectrogram as a greyscale image. The following sections will discuss the basis of this transformation.

3.1.1 Spectrogram-Moiré Image Analogy

Optical measurement methods of three-dimensional surface metrology became rapid and practical tools, especially in the field of orthopaedics [97–99, 106–109] where Moiré imaging (used primarily on spinal deformities) is considered to be capable of measuring and graphically displaying whole surfaces instantaneously. A new structure arises with more extended periods by superimposing two similar periodic structures translated or rotated relative to each other. This one is called the Moiré pattern, and it consists of the Moiré fringes. Simple Moiré patterns can be observed when superposing two transparent layers comprising periodically repeating opaque parallel lines as shown in Fig. 3.1a [100]. The lines of one layer are parallel to the lines of the second layer.

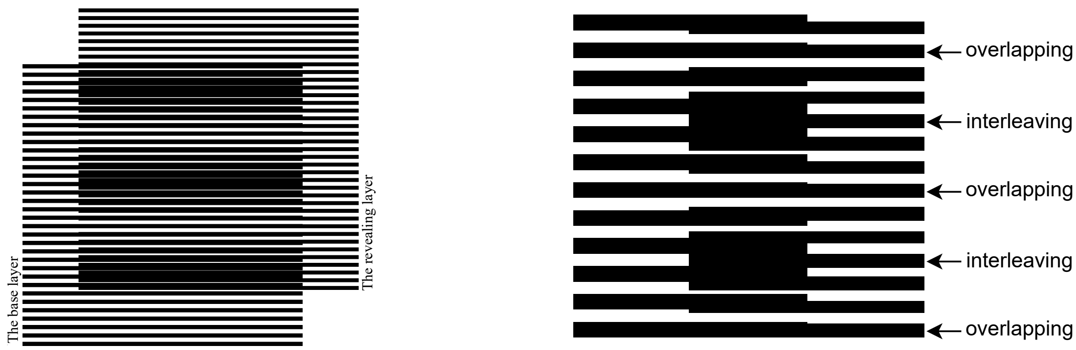

(a) Basis of the Moire method (b) Superposition of two parallel layers

Figure 3.1: Illustration of the Moiré method [100]

The superposition image does not change if transparent layers with their opaque patterns are inverted. One of the layers is denoted as the base layer and the other as the revealing layer (Fig. 3.1a). The superposition image of Fig. 3.1a outlines periodically repeating dark parallel bands, called Moiré lines. Spacing between the Moiré lines is much larger than the periodicity of lines in the layers. Light areas of the superposition image correspond to the zones where the lines of both layers overlap. The dark areas of the superposition image forming the Moiré lines correspond to the zones where the two layers interleave, hiding the white background. The labels of Fig. 3.1b show the passages from light zones with overlapping layer lines to dark zones with interleaving layer lines. The light and dark zones are periodically interchanging [100]. The main objective of the research was to find out how to extract information from spectrograms more efficiently and reliably without losing any information. As the spectrogram was able to correspond to a map where the third dimension is represented with colours or colour-densities, it was possible to correlate it to a Moiré-image. In this aspect, the black "Moiré" lines could represent the exact frequency component trends and the basis of the next steps of the research. There have been numerous studies [96–99] conducted on Moiré-image evaluations.

3.1.2 Spectrogram Conversion to Image Space

During the research, in addition to this Moiré-image analogy, vibration information could be kept lossless as the spectrogram was exported as a greyscale normalised image. The amplitude values were normalised along with the black-white pixel values stored in one byte with integer values between 0 and 255, ensuring the preservation of the information as the tendency of the TF ridges is important only. The absolute amplitude values will be in the focus when the inverse transformation from image-space is carried out at the end of the image evaluation sequence. An additional advantage of this process is the more utilised computational resource usage due to the data compression of the image generation. Unnecessary information from the spectrogram graph, such as scaling, axes etc., needs to be eliminated to provide a reliable source for the image evaluation process. Therefore, the images were produced fixed resolution during the method with 800x800 pixels. Furthermore, it is crucial to prevent major information loss on the STFT properties as the data from the image-space needs to be transferred back to the TF domain later on. For later steps the characteristics and tendency of the frequency lines are needed, not the exact amplitude values. The collected information was exported to an auxiliary file by the spectrogram image, which contains the time and frequency range, the time and frequency resolution, the number of pixels in the time and frequency range, and the amplitude range enabling the spectrogram reproduction at any time. For example, in Simulation Setup 2 in Table 2.3, the given amount of pixels is equal to 12.5 Hz, and 0.031 s in the case of a greyscale image. The pixel values represent the amplitude in $\frac{\mathrm{V}^2}{\mathrm{Hz}}$.

3.2 Theoretical Basis

In the previous section, the spectrogram greyscale image was created. In this chapter, image preparation and evaluation methods will be demonstrated, and then further will be used to extract the vibration signal's frequency component information of a rotating machine from a spectrogram image.

When the STFT was performed, the spectrogram image is available for further analysis. Before the extraction of frequency components, additional image pre-processing method applications are recommended to emphasise the relevant information content of the image. In image processing, various well-known methods can be applied, such as point-to-point operations, local or global operations. During the research, the spectrogram was exported from that part of the signal, which contains the most relevant information about operational states (e.g. a ramp-up or constant sections) with the possibility of further image manipulation.

In global operations the new brightness of a given pixel depends on all other points in the image. The starting point for the transformations was the image plane and was performed only on those visible pixels. However, global operations are based on a range of plane functions where the components change the amplitude and phase components, which affects the whole picture. In the studies, the Fourier transform of the image was determined. By filtering, amplifying and attenuating the individual components of the obtained result, the images were changed according to the requirements for the test. However, the changes take effect only if we perform the inverse Fourier transform on the data afterwards. The result is the changed image. The methods allow for a deeper examination of objects. However, this method has the greatest computational requirement among the operations since all the image points play a role. The time required for the calculation can be reduced by using the fast Fourier transform.

In local operation solutions the new brightness of a given pixel is affected by its original brightness and the specified environment (for example, 3×3 pixels). The point thus determines the new brightness and its environment and the used transformation method. Operations include convolution-based rank filtering. Convolution means the weighted sum of the brightness of a pixel and the points around it. The method makes it possible to clean noise-laden images, highlight and sharpen edges with the help of various operators (windows). The computational requirements of the operations are proportional to the number of pixels and the size of the pixel environment, i.e., N^2P^2 (assuming an image of NxN pixels and a test environment of PxP pixels).

Finally, in point-by-point operations, the new brightness of a given pixel is only affected by the original brightness of that point, i.e., the result is independent of the other pixels, and their results are collected in a table. When examining points in an image, the results for that point are retrieved and assigned from this table. In a broader sense, these transformations include creating new images created by arithmetic or logic operations based on the brightness values of points at two positions in two images of the same size. These include histogram transformations, including inversion, elimination, and colouring. The computational requirement of the operations is proportional to the number of pixels, i.e., N^2 (assuming an image of NxN pixels).

In the following section, example methods for these three operation type will be discussed which are the histogram manipulations and filterings.

3.2.1 Image Histogram Manipulation

An important method of examining images is to analyse their histogram. The histogram shows the frequency of occurrence of each value. In this case, it can be found out which colour appears most or least in the given image. Based on the information, the pixels' values can be manipulated to display, for example, a smaller amount of a point of the selected colour in the image, thereby improving its contrast.

Two histogram-based studies were performed during the research. In the first case, contrast enhancement can be performed on the image, i.e. a histogram compensation. In this case, knowing the image histogram, the correction method makes the brightness codes evenly distributed. The use of the method is advantageous for less contrasting images, i.e. the intensity values are concentrated in a minor part of the intensity range.

During the second case, which is the so-called binarisation method, the pixels of a given image are transformed so that, in the end, they can only take one of two values. After the transformation, the essential darker parts are highlighted, while the irrelevant parts are suppressed.

However, the images used to test the methods showed that the method is not necessarily suitable for the correction and analysis of spectrograms. This is because the vibration signals are usually too noisy for the image generated during binarisation to detect time-dependent changes. The edges representing these are blurred with the noise and could not be highlighted or analysed.

(a) Original image (b) Histogram Correction (c) Binarisation

Figure 3.2: Illustration of Histogram correction and binarisation on a greyscale spectrogram

For the above reasons, a third possibility was chosen in which three factors are influencing the contrast of the image. This is the Brightness-Contrast-Gamma (BCG) correction method. By adjusting the brightness, the brightness of the image can be increased or decreased, while by changing the contrast, the brightness ratio between the light and dark parts can be adjusted. Gamma is a correction value that allows changing the brightness of pixels and the sharpness of their colours. In the rest of the research, this BCG correction method was used. Examples of the different histogram manipulation results on a greyscale spectrogram image can be seen in Fig. 3.2 while Fig. 3.3 and Fig. 3.4 represent some corner cases of the BCG correction.

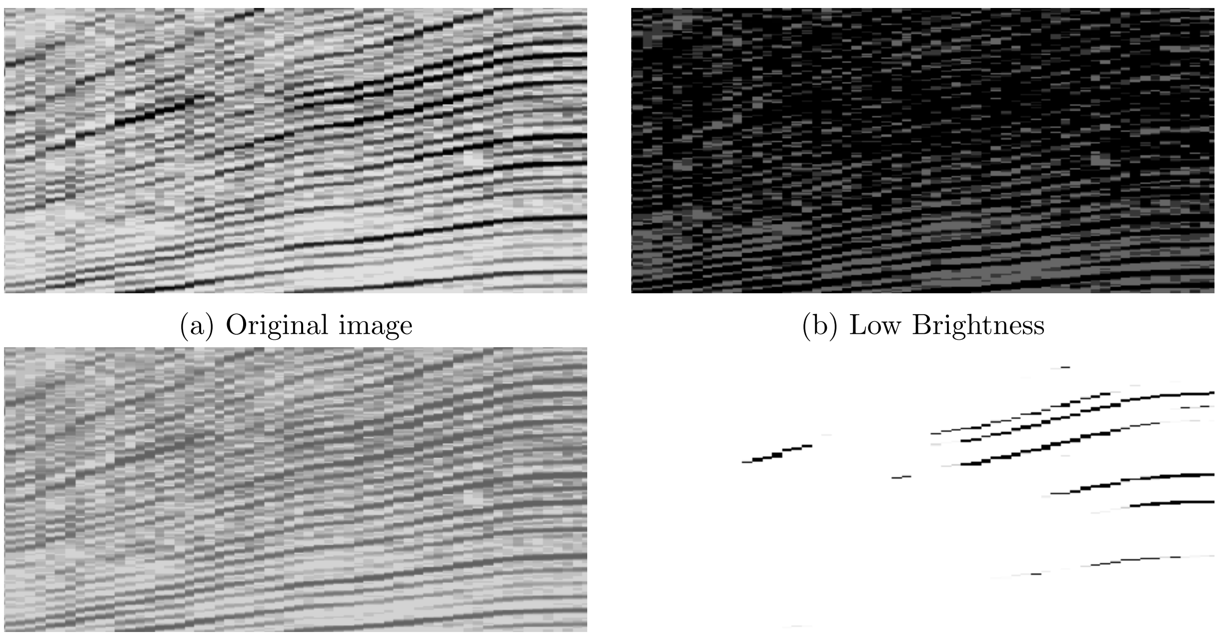

(a) Original image (b) Low Brightness

(c) Low Contrast (d) Low Gamma

Figure 3.3: Illustration of low Brightness-Contrast-Gamma correction parameter effects on a greyscale spectrogram

3.2.2 Image Filtering

In image processing, filtering can be considered as a mask or window-based transformation. During the process, each pixel changes depending on what points are in its vicinity. The size of the original one and the image obtained after filtering are the same in all cases. The method goes through each pixel one by one, one after the other. The masks used for filtering are represented by matrices, the values of which are called weights. These are usually quadratic

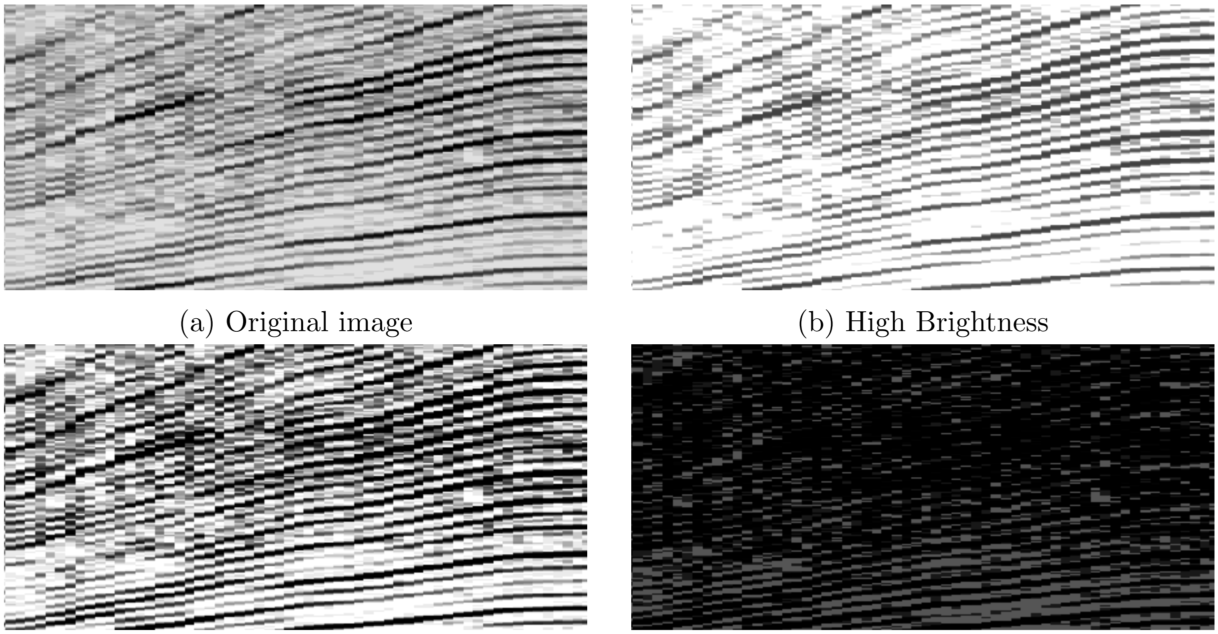

(a) Original image (b) High Brightness

(c) High Contrast (d) High Gamma

Figure 3.4: Illustration of high Brightness-Contrast-Gamma correction parameter effects on a greyscale spectrogram

matrices of an odd size, thus having a centre, an origin. In the simplest case, these masks are linear, i.e., the given pixel is replaced by a linear combination of its surroundings according to the weights of the mask. In this case, the matrix is also called a convolution kernel or mask, as shown in Eq. 3.1.

$$\begin{vmatrix} 1 & 7 & 3 \\ 1 & 2 & 5 \\ 10 & 9 & 8 \end{vmatrix} \otimes \begin{vmatrix} 1 & 1 & 1 \\ 1 & 8 & 1 \\ 1 & 1 & 1 \end{vmatrix} = \begin{vmatrix} 0 & 0 & 0 \\ 0 & 60 & 0 \\ 0 & 0 & 0 \end{vmatrix} \tag{3.1}$$

For the evaluation and analysis of different filtering methods, references [105, 110–113] were used. See these references for more detailed information.

The exported greyscale spectrograms were contaminated with noise. From the point of view of image processing, eliminating them is an common challenge. At the beginning of the research, it was unknown which method could produce the best result, so several methods were examined which are represented in Fig. 3.5.

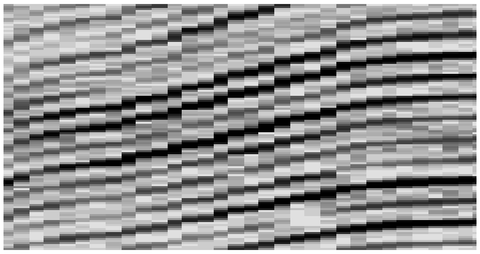

(a) Original image

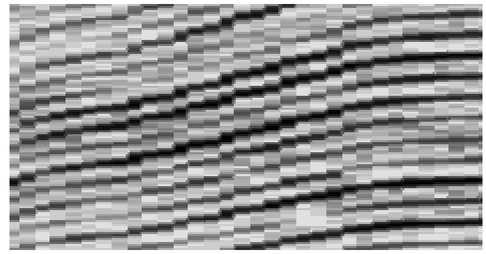

(b) Low-pass filtering

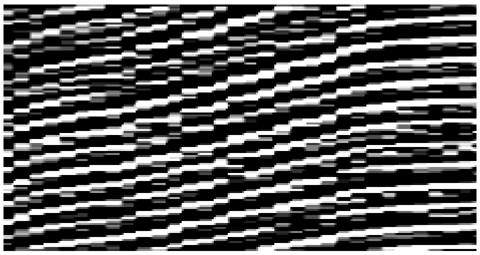

(c) Convolutional filtering with Gradient-kernel

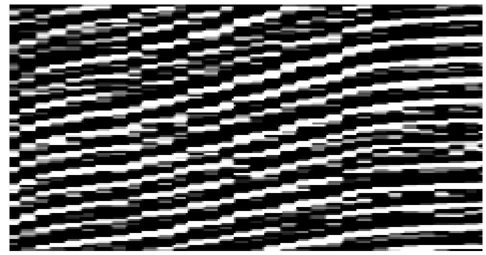

(d) Convolutional filtering with Laplace-kernel

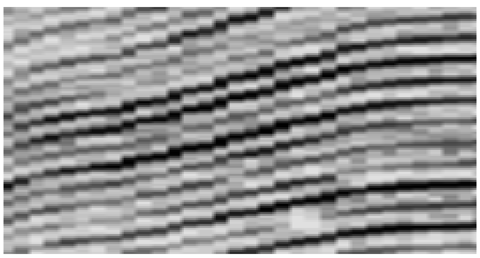

(e) Convolutional filtering with Smoothing-kernel

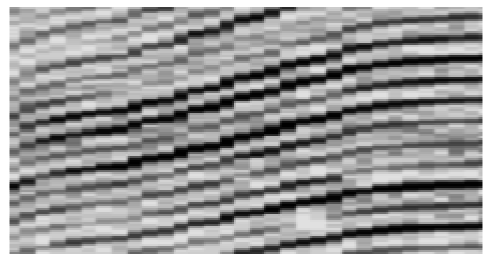

(f) Convolutional filtering with Gauss-kernel

Figure 3.5: Illustration of filtering methods on a greyscale image

- *Low-pass filter:* When a low-pass filter is used, high-frequency parts of the frequency range are damped or eliminated, causing the image to be blurred. Testing of the option revealed that the processability of the spectrograms could not be significantly improved.

- *Convolutional filter:* For convolutional filters, four different types of kernels can be chosen. In each case, a pre-built matrix of 3×3, 5×5, or 7×7 elements can be used to filter the image.

  Gradient-kernel: Using a gradient filter, we approximate the x and y gradients of the derivatives taken at points in the image as surfaces by the difference quotient. With the method, significant intensity changes and edges can be detected because it eliminates homogeneous areas.

Laplace-kernel: Laplace filters are based on the second derivative of x and y at a given point. In practice, the method is the difference between the smoothed and the original version of the image, due to which it reacts significantly to changes in intensity, i.e., edges and errors.

Smoothing-kernel: Smoothing filters are determined by the average of the points in the vicinity of a given point. Accordingly, the window contains only positive values. The degree of smoothing is determined in each case by the size of the mask used. Smoothing kernels act as a low-pass filter and can be used to eliminate various noises and blur images. The downside is that it also removes fine detail from the image.

Gauss-kernel: Gaussian filters work similarly to smoothing kernels, except that they are calculated differently. The modified value of a given pixel can be derived from the pixel's weighted average in its vicinity in the former case. The degree of smoothing is determined here by the distribution. The values of the mask are circularly symmetrical or close to zero at its edge.

- N^{th} *order filter:* The N^{th} order filter also corresponds to a low-pass filter. The point is that the modified value of a given pixel is given by the points around it, where the basis of the study is a quadratic matrix of odd size defined by us. The covered points are queued by the filter based on their values, and the N^{th} value of this queue will be selected as the new value of the examined pixel. The total light intensity of the image can be adjusted by selecting N since selecting a high-value result in a lighter image and vice versa.

- *Morphological filter:* By applying morphological filtering, the shape of different regions can be changed by increasing the light areas at the expense of the dark ones, which can also be realised backwards. Different types of filters smooth the image based on the patterns and increase the contrast in the border areas.

Some results showed that quality improvement could be achieved using morphological filters; therefore, further evaluation was performed in this filtering family. Briefly, the following morphological filter types were evaluated which are represented in Fig. 3.6.

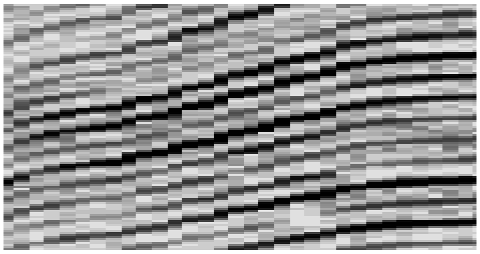

(a) Original image

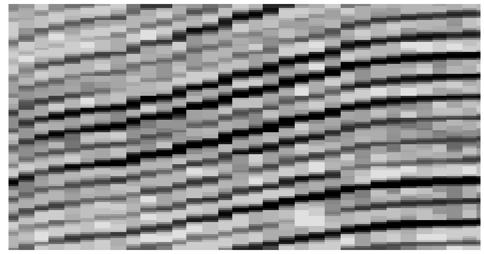

(b) Erosion filtering

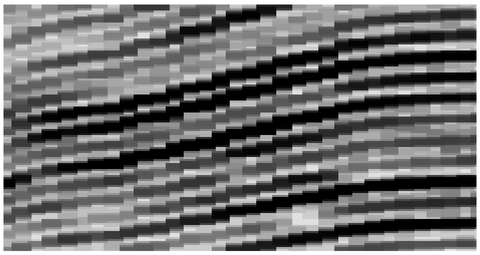

(c) Dilatation filtering

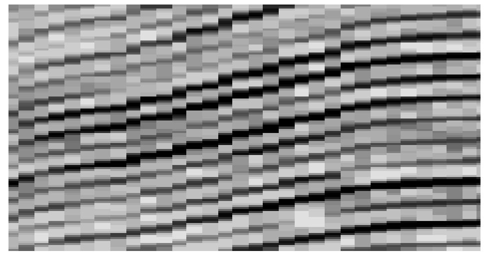

(d) Opening filtering

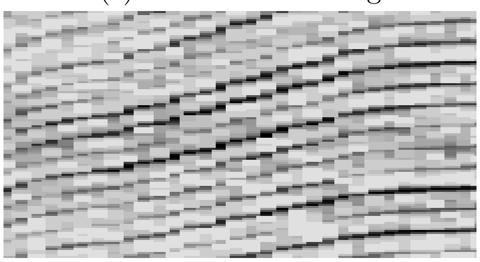

(e) Closing filtering

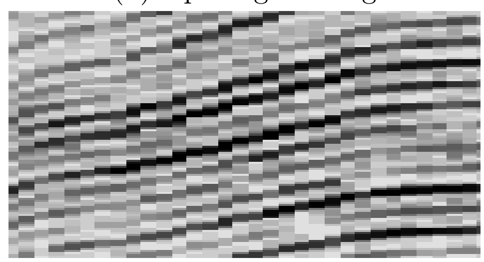

(f) Auto-median filtering

Figure 3.6: Illustration of morphological filtering methods on a greyscale image

- *Erosion filter:* During erosion, the brightness of pixels surrounded by lower intensity points is reduced.

- *Dilatation filter:* Dilatation has the opposite effect to erosion, i.e., it increases the brightness of the pixels if the intensity of the points around is higher. In the process, brighter regions expand at the expense of darker ones.

- *Opening filter:* Opening consists of the successful running of two processes, i.e., the execution of erosion is followed by dilatation. The method essentially removes bright spots that are in a dark environment and smooths out individual borders. However, in the process, the size and shape of each region do not change significantly, as erosion and dilation are morphological opposites of each other.

- *Closure filter:* Closure is the opposite of opening because the same two processes take place only in reverse order. The course of dilatation erosion removes dark spots found in light environments and smooths out individual borders.

- *Auto-median filter:* The Auto-Median function occurs as a double combination of openings and closures, resulting in simpler regions with less details.

It can be seen that the different morphological filters have their advantages and disadvantages as well. It was not the scope of the actual research to determine which filtering method is the best solution for vibration signal evaluation because it depends on the signal under evaluation, the setup on the measurement system and the characteristics of the applied sensor.

As a summary, it can be said that the information content of the image can be highlighted better if a low-pass or convolutional filter with Gauss-kernel or morphological dilatation/erosion filter was applied on the spectrogram. Additionally, the combination of these filters by executing them one after the other can enhance the results also.

3.3 Proposed Spectrogram Image Preparation

Before moving forward in the evaluation steps, additional image pre-processing methods are recommended to be applied on the spectrogram. With these, the necessary information about the frequency components could be better emphasised. During our research, the spectrogram was exported from that part of the signal, which contains the most relevant information about operational states (e.g. a ramp-up or constant sections), but the image may have to be manipulated further.

With the intention to accomplish this manipulation, the following image processing methods were utilised. Based on our basic research, we can recommend the order and parameters of the used methods, whereas the influence of the recommended order and parameters on the final results requires further research. The evaluation started with BCG correction using parameters $B = 171, C = 56, G = 1.51$ followed by a histogram correction and a convolutional 6×6 Gaussian filter. Additionally, several other methods could be applied like low-pass, morphological, erosion, dilatation filtering, image binarisation and so on, to improve image quality. More-in-depth details can be found in references [112, 114, 115] about the generally

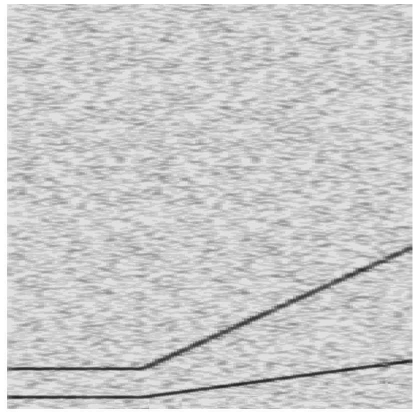

Figure 3.7: Exported greyscale spectrogram of Simulation Setup 6 in Table 2.4.

used filters and correction techniques applied in image processing. An example image after correction methods can be seen in Fig. 3.7.

It has to be highlighted that this sequence of steps is general, but the parameters depend on the vibration signal itself because of the possible different sampling frequency rates and various types of noises. The parameter optimisation of these steps to ensure signal quality independence is outside of the scope of this paper. It can be assumed that filtering and signal conditioning was performed correctly before STFT image creation.

The methods, presented so far, reduced the amount of noise on the image and highlighted the essential details of the image better.

3.4 Edge Detection

After the image preparation is performed, the evaluation of the content can come. During this evaluation additional image related actions will have to be executed in order to obtain the frequency components from the spectrogram. As a pre-requirement for the next steps, we have to declare that frequency component intersections do not exist because f_k frequencies of every rotating part of the construction depend on the primary $f(n)$ RPM.

In the beginning, auxiliary mesh generation and edge detection are necessary to find those points which can be part of a frequency component on the image. The algorithm creates several parallel, vertical auxiliary grid lines in the image in the first step of the detection, based on an adjustable line-density setting in pixels. These mesh lines intersect the frequency lines (black lines), so rising and falling edges will be detectable on the image.

With a rare mesh, the ridges can be lost. They can flow into each other, making them difficult to process. Their intensity may vary along each edge, so there may be sections that can not be detected. In the case of a dense mesh, such sections can distract from finding an otherwise visible edge. The effect described above is shown in Fig. 3.9 and Fig. 3.8. For the above-specified greyscale spectrograms an auxiliary mesh with a resolution of 10 pixels or more is optimal.

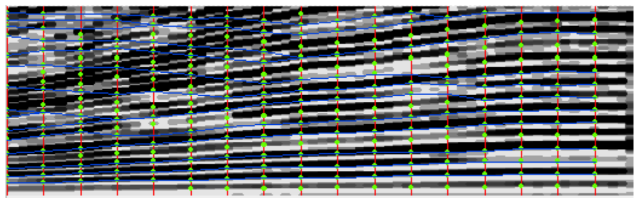

Figure 3.8: Rare vertical auxiliary mesh lines (red - vertical mesh lines, black - frequency components, green points - found edges)

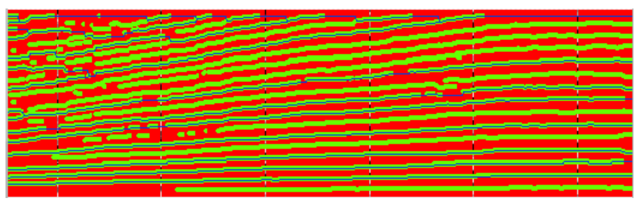

Figure 3.9: Dense vertical auxiliary mesh lines (red - vertical mesh lines, black - frequency components, green points - found edges)

In order to find the edges where mesh lines and frequency components intersect each other on the spectrogram image, it is cardinal to determine from which direction we are looking for them. With a setting called edge polarity, it can be specified where the edge detection starts along a given line. In most cases, the boundary between a light and a dark area marks the edge of a shape. In the present case, a detected point indicates the edge of the edge, which also has another side, for test purposes that can be selected which boundary point of the found shape to display along the mesh line passing through it. The test is most optimal when the lower edges (Rising Edges) are displayed when searching for rising edges, while the upper points are displayed when searching for rising edges. The effect described above is shown in Fig. 3.10a and Fig. 3.10b. It is important to note that in the case of an image from which a polygonal area has been removed, the masked section's boundary may also interfere with detection.

Another important setting for filtering edges is the pixel strength of the searched element. In essence, it can be specified how significant the intensity of the areas should be to qualify

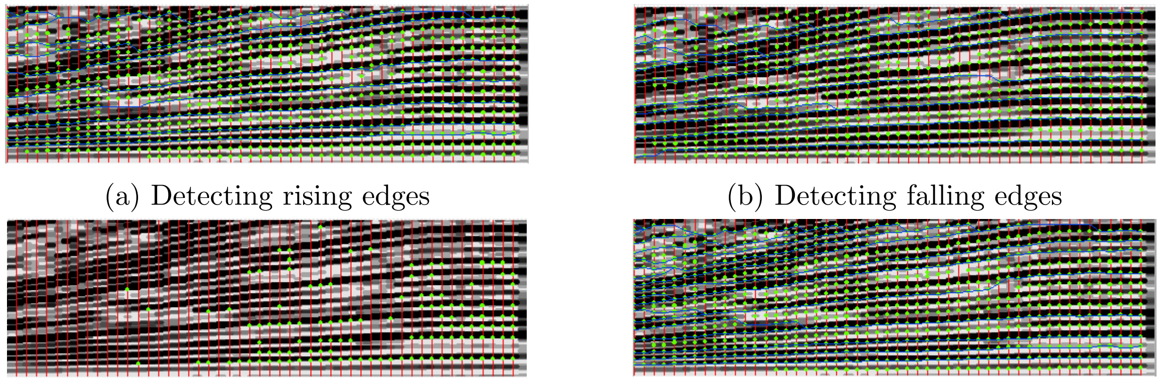

(a) Detecting rising edges

(b) Detecting falling edges

(c) Detection with high intensity difference

(d) Detection with low intensity difference

Figure 3.10: Edge detection with different setups – (red - vertical mesh lines, black - frequency components, green points - found edges)

it for a light and dark area border. From this, it can be concluded that using low intensity threshold values will result in irrelevant points, while significant edges may be lost at high intensity threshold values. The effect described above is shown in Fig. 3.10c and Fig. 3.10d.

As an optimal auxiliary mesh generation result for one Simulation Setup can be seen in Fig. 3.11.

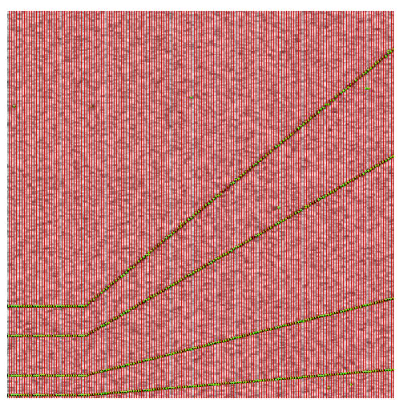

Figure 3.11: Generating vertical auxiliary mesh lines on the spectrogram image obtained from Simulation Setup 2 in Table 2.3 (red - vertical mesh lines, black - frequency components, green points - found edges)

As it was mentioned before, the black lines indicate a frequency component on the image. The method checks coherent rising and falling edges to get the most reliable result and calculates the average vertical pixel coordinate. Thus, if the black line is thicker, the frequency component is dominant, the middle of this line can be found. After this, an intersection point can be inserted, representing one point of a frequency component. These intersection points are only visually capable of representing one frequency component. In order to capture a processable result, so-called component tracking algorithms were implemented. These can link those coherent points to each other during a horizontal sweep through the auxiliary grid lines, which belong to one frequency component. These methods will be introduced in Chapter 4.

Chapter 4

Vibration Information Extraction from Spectrogram Image

During the previous chapters, the STFT method and the spectrogram creation was in the foreground, followed by the theoretical basis of image processing and the used image preparation methods for frequency ridge evaluation.

The main target is to obtain the vibration frequency component information from the spectrogram image, which can be achieved using so-called component tracking methods. These methods will be introduced during the sections with their calculation background supplemented by their advantages and disadvantages illustrated on the example simulated signals discussed in Chapter 2.

The final part of this chapter will give an overview of how the obtained information can be transferred back to the frequency-time domain from the image domain to support rotary machine diagnostics and condition monitoring tasks.

The main content of Chapter 4 is based on the relevant references [11, 116, 117].

4.1 Component Tracking Methods

The following sections will contain the theoretical description of the component tracking methods extended with test and evaluation on simulated signals.

4.1.1 Differential Method

In order to connect the detected intersection points, first, the so-called Differential Tracking Method (DTM) was developed.

The detectable intersection points ($j = 0...M$) along a vertical grid line and a frequency component line in the spectrogram are represented by green dots, the mentioned grid lines $i = 0...N$ shown in red in Fig. 4.1. The connection of these points starts with a point along the first vertical line (Fig. 4.1a). These points are handled as an initial point $P_{i,j}(x_{i,j}; y_{i,j})$ of a new frequency component on the image where x is the pixel coordinate along the horizontal axis, and y is the pixel coordinate along a grid line.

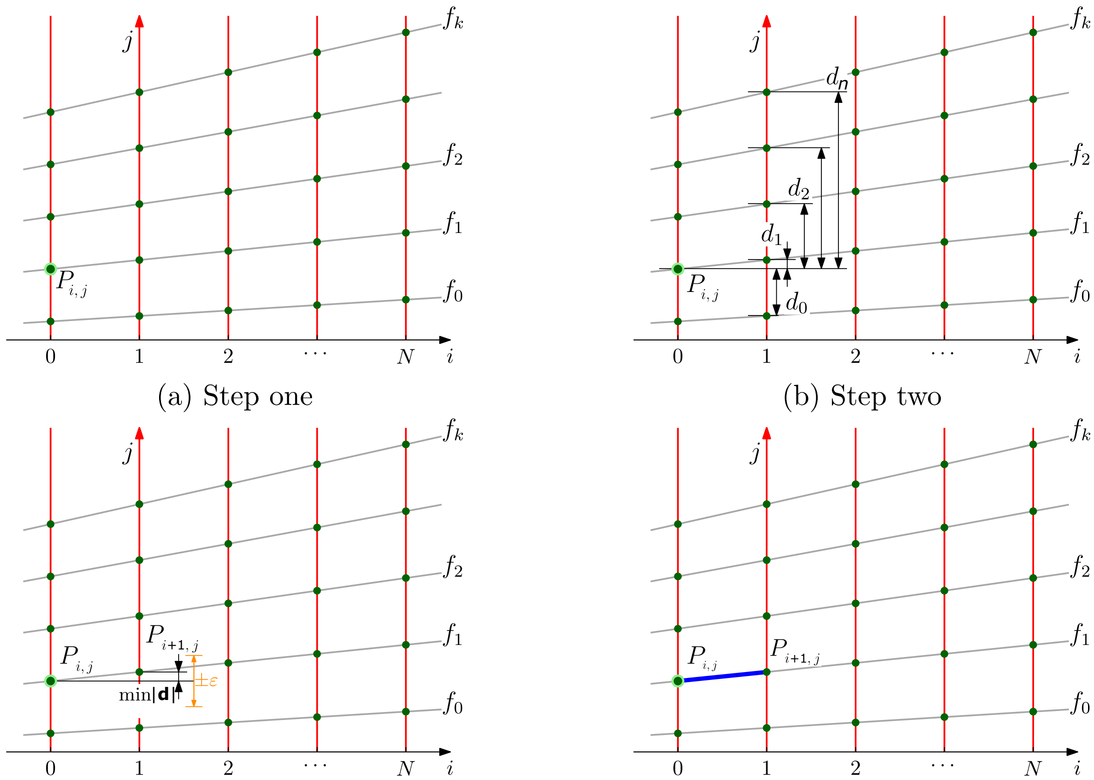

(a) Step one (b) Step two (c) Step three (d) Step four

Figure 4.1: The steps of the DTM – (grey - spectrogram lines, red – vertical mesh lines, green – found intersection points with spectrogram lines, light green – indicator of the initial point, orange - tolerance range, blue - found segment of a frequency component)

After finding the initial points, the algorithm calculates the vertical distance between (Fig. 4.1b) the starting point and the detected points on the following line of the auxiliary grid as

$$\mathbf{d}_n = y_{i+1,n} - y_{i,j}, \tag{4.1}$$

where $\mathbf{d}$ is the vector of the calculated vertical differences, $y_{i+1,n}$ is the y coordinate of an intersection point on the $i+1$ vertical grid line and n is a running index which iterates over the elements of j. From the calculated differences the algorithm chooses the minimum absolute value and performs further examination on the detected $P_{i+1,j}$ point (in Eq. 4.2).

If $P_{i+1,j}$ in Fig. 4.1c is inside a pre-defined ε tolerance range, the software assumes that this is the next element of the currently analysed k frequency component. This tolerance range (indicated with orange in Fig. 4.1c) is based on pixel values related to the frequency resolution of the STFT spectrogram creation method. This correspondence can be made based on the available vertical frequency and image pixel resolution from the greyscale image export. If all of the differences in the collected vector are outside of the ε range the detection of the k frequency component ends, then the algorithm jumps to the next i vertical line. The same routine is executed if along a grid line edges were not detected. If the calculated difference value is between the tolerance limits, the logic saves this point as the new element of the frequency component indicated with blue in Fig. 4.1d. These above-mentioned steps are described by the following equations

$$P_{i+1,j}(x_{i+1,j}; y_{i+1,j}), \tag{4.2}$$

where

$$x_{i+1} = x_i + \Delta_{mesh}, \tag{4.3}$$

$$y_{i+1,j} = y_{i,j} + \min|\mathbf{d}| \quad \text{if} \quad \min|\mathbf{d}| \leq \varepsilon \tag{4.4}$$

or

$$y_{i+1,j} = y_{i,j} \quad \text{if} \quad \min|\mathbf{d}| > \varepsilon, \tag{4.5}$$

where $P_{i+1,j}$ is the closest point based on differences; Δ_{mesh} is the difference between two vertical mesh lines; $\min|\mathbf{d}|$ is the minimum absolute value in the $\mathbf{d}$ vector and ε is the tolerance in pixels. As the result of the tracking algorithm the found frequency components are collected into an $\mathbf{f}_k$ vector.

After the previous step, the algorithm restarts with the last $P_{i+1,j}$ point as an initial point and analyses the intersection points on the following line of the grid. In the next iteration, those points on the upcoming grid line, which were not taken into account in the previous step, become initial points. This searching process will be repeated until the algorithms examine all grid lines one after the other until the image's border or the next found intersection point is outside of ε tolerance. When every vertical line was analysed, the results will be represented as found frequency components. If any intersection occurs between the found frequency components during evaluation, the algorithm will terminate the execution and returns with the intersection information. The operation of the algorithm can be influenced significantly by two customisable, independent parameters. The first is the above-mentioned adjustable line-density setting in pixel values; the second is the tolerance range during the differential search.

Tests showed that a too dense (mesh line density is 1 pixel) or too rare grid (mesh line density is higher than 20) provide bad results, which means the components detected by the algorithm were distorted or false. During the evaluation, the resolution was 5 pixels, ensuring that the change of rotating speed does not influence the tracking method using the defined image resolution.

4.1.2 Moving-Average-Predictive Tracking Method

As a next step, the previously introduced differential method was improved further. The so-called Moving-Average-Predictive Tracking Method (MAPTM) method in Fig. 4.2 estimates vertically where the next point of the actual frequency component has to be located on the following grid line and takes it as the initial point of the logic.

$$\tilde{P}_i(\tilde{x}_i;\tilde{y}_i), \tag{4.6}$$

where

$$\tilde{x}_i = x_{i,j}, \tag{4.7}$$

$$\tilde{y}_i = y_{i,j} + \tilde{\delta}, \tag{4.8}$$

where $\tilde{\delta}$ is a predictor value, calculated by

$$\tilde{\delta} = \frac{\sum_{n=0}^{i} \mathbf{D}_n}{\dim(\mathbf{D})}, \tag{4.9}$$

where

$$\mathbf{D}_i = \min |\mathbf{d}|. \tag{4.10}$$

This logic is represented in Fig. 4.2b. In other words, the improved method is a gradient-based probability estimation, but the main algorithm steps remain the same.

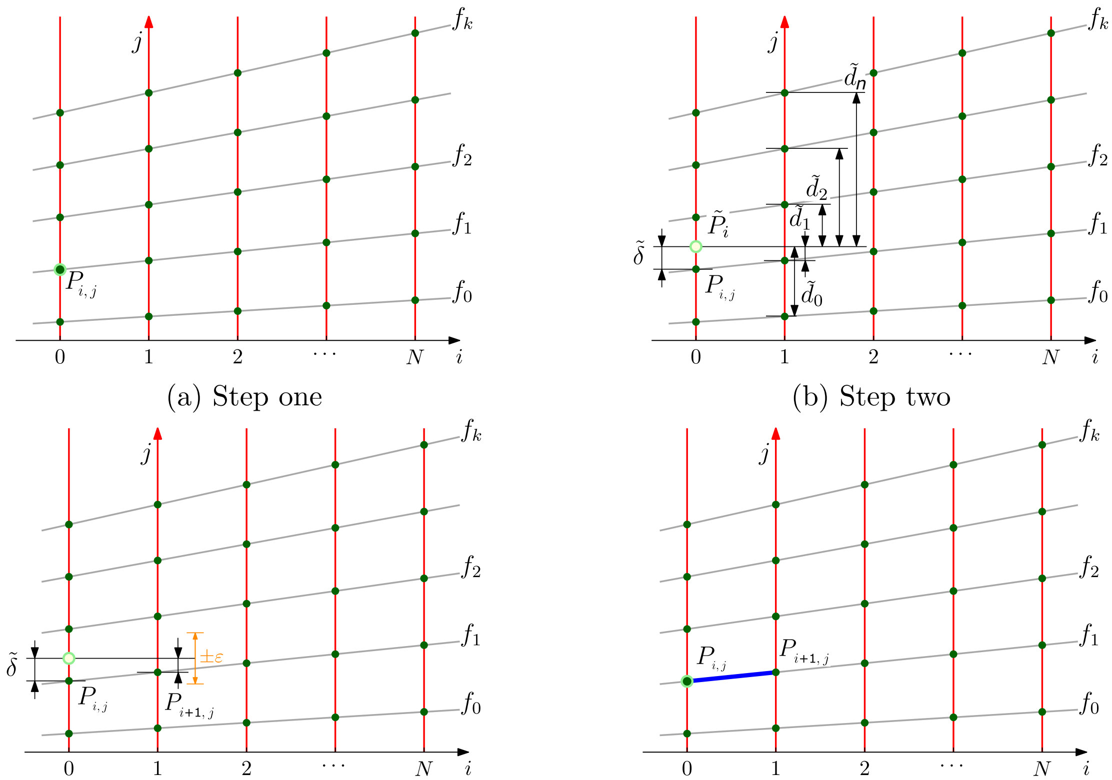

Figure 4.2: The steps of the MAPTM – (grey - spectrogram lines, red – vertical mesh lines, green – found intersection points with spectrogram lines, light green – indicator of the initial point, orange - tolerance range, blue - found segment of a frequency component)

The algorithm collects in the $\mathbf{D}$ that information from the k found frequency component line what the previous difference values during the component tracking were and calculates the average of this vector in every iteration. This is the so-called $\tilde{\delta}$ predictor value. In the next step, shown in Fig. 4.2c, the vertical coordinate of $\tilde{P}$ is adjusted with this predictor value. During the first iteration, $\tilde{\mathbf{d}}_\mathbf{i}$ always has a value of zero. Based on this corrected initial point, the logic sweeps through the points like the differential method on the next grid line. That $P_{i+1,j}$ point will be the next element of the frequency line of which vertical $\tilde{\mathbf{d}}_i$ difference value from vector $\tilde{\mathbf{d}}$ is inside the ε tolerance. Like mesh dependency and stop criterion, every other property of this tracking algorithm is the same as what mentioned above in the differential method. This MAPTM method is based on the following equations.

$$\tilde{\mathbf{d}}_n = y_{i+1,n} - \tilde{y}_i \tag{4.11}$$

$$P_{i+1,j}(x_{i+1,j}; y_{i+1,j}), \tag{4.12}$$

where

$$x_{i+1} = x_i + \Delta_{mesh}, \tag{4.13}$$

$$y_{i+1,j} = \tilde{y}_i + \min|\tilde{\mathbf{d}}| \quad \text{if} \quad \min|\tilde{\mathbf{d}}| \leq \varepsilon \tag{4.14}$$

or

$$y_{i+1,j} = y_{i,j} \quad \text{if} \quad \min|\tilde{\mathbf{d}}| > \varepsilon, \tag{4.15}$$

where $P_{i+1,j}$ is the closest point based on differences between the predicted point and the found points; $\min|\tilde{\mathbf{d}}|$ is the minimum absolute value in the $\tilde{\mathbf{d}}$ vector and ε is the tolerance in pixels. If all of the differences in the collected vector are outside of the ε range the detection of the k frequency component ends and the algorithm jumps to the next i vertical line.

In Fig. 4.3 an evaluated spectrogram image derived from Simulation Setup 2 in Table 2.3 can be seen after executing the MAPTM method. This method with the averaged edge detection is more precise due to its logical behaviour. [70] represents a closely similar method, but in this research, the image itself was used to transfer the tendency information with greyscale representation. This simplified and accelerated the evaluation process; besides, it made it possible to directly represent the 2-D TF representation described in the next section.

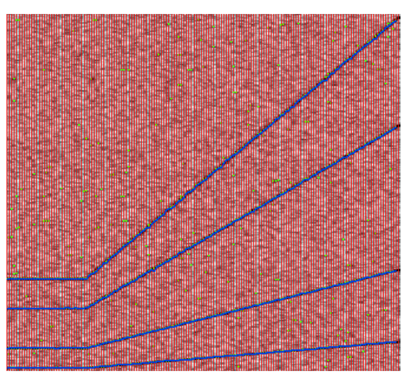

Figure 4.3: Spectrogram image after the execution of the MAPTM method in case of Simulation Setup 2 in Table 2.3 (red - vertical mesh lines, black - frequency components, green points - found edges, blue - result of the component tracking)

4.2 Image to Vibration Space

After the algorithm found several component ridges on the image, the next step is to convert the results back into the TF domain. The bases of this transformation are the parameters exported parallel with the greyscale spectrogram export at the end of the vibration signal processing. Based on those resolution parameters, the detected lines can be transferred back to exact frequency components. The detected lines on the images need to be post-processed because of the frequency resolution problem of the spectrogram and to provide a more processable form for other rotating machine diagnostic methods. It should be pointed out that during this step, the algorithm eliminates the false frequency line detections, which means, lines without specific ending - do not meet the end of line criterion discussed in the previous section - will be removed. It occurs when the tracked line breaks somewhere along with the image or merges into another tracked line.

The basis of the post-process method is a sliding windowed logic - which was also used during the STFT spectrogram creation to split into segments as the input for the DFT - where the input parameters are the window width and the overlap in seconds. The values of these parameters are the same used as time resolution parameters during the STFT spectrogram creation to ensure that time lag or distortion cannot influence the results.

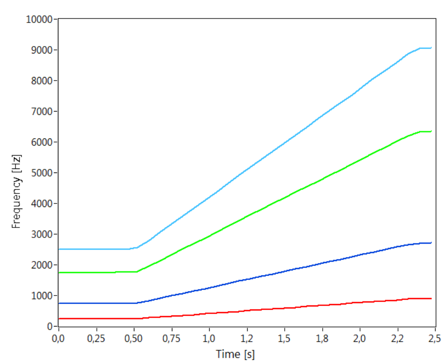

Figure 4.4: Obtained frequency components from the spectrogram image after back-transformation (colours represent the found components) in case of Simulation Setup 2 in Table 2.3

The next step is the main post-process algorithm. A point-by-point smoothing method can estimate whether the detected frequency component is constant or variable over time by calculating the primary gradient of the signal. Therefore, similar to the above interpreted predictive tracking algorithm, a prediction value was applied. Hence, the same predictive method was used for post-processing to obtain the transient frequency component results extended with sliding windowing. Fig. 4.4 demonstrates the operation of the method by an example of the frequency components of a simulated signal as a result after image evaluation and back transformation with the point-by-point smoothing. These results can be used for condition or fault analysis when the construction of the rotating machine is well known. In this case, the extracted frequency components can be corresponded to the relevant machine elements.

As a summary, Fig. 4.5 represents the main steps of the proposed hybrid method evaluating a simulated signal.

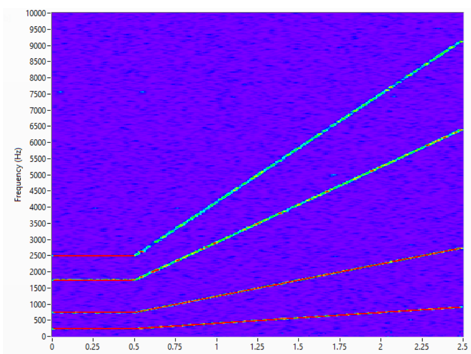

(a) STFT spectrogram

1

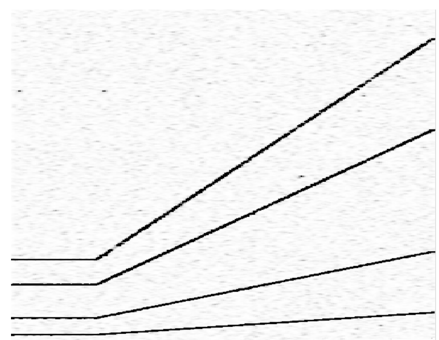

(b) Greyscale spectrogram

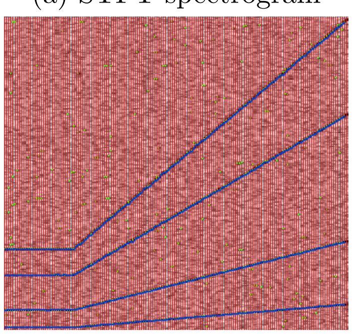

(c) Component tracking

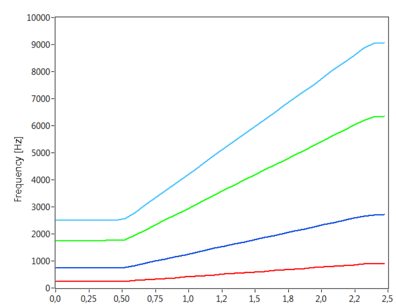

(d) Information extraction

Figure 4.5: Demonstration of the hybrid method steps on the signal of Simulation Setup 2 in Table 2.3

4.3 Novel Results

In this section those novel results will be summarized which are related to the part of the research work presented in Chapter 4.

4.3.1 Thesis 2

Method steps for information extraction from a greyscale vibration spectrogram image

Frequency components of the power spectra spectrogram resulted from the commonly used Short-Time Fourier Transformation method used in rotating machine diagnostics can be detected using image processing methods. Both stationary and transient components in a vibration signal can be detected by converting the spectrogram into a greyscale image, performing the following sequence of steps.

1. Short-Time Fourier Transformation execution with the enhanced algorithm with a time resolution, not less than the estimated time period and a frequency resolution as high as possible.
2. Conversion of the resulted spectrogram into a greyscale image.
3. Elimination of noisy and information-irrelevant areas with image manipulation methods.
4. Generation of an auxiliary raster grid on the greyscale image.
5. Edge detection - obtaining the intersection points of possible frequency ridges and the vertical auxiliary grid lines.
6. Linking the found intersection points with the differential (extreme value-based) or moving-average prediction (gradient-based) component tracking algorithm.
7. Conversion of the found frequency ridges found in the greyscale image to the time-frequency plane.

8. Smoothing the converted results for further evaluations using averaging or point-by-point windowed filtering.

Related publications: [MG1, MG2, MG3, MG4]

4.3.2 Thesis Group 3.

The following theses are mainly related to the previously presented thesis, describing the order of steps of the hybrid method. In addition to the general description of the process, however, a few steps should be highlighted that form an essential part of the method.

Thesis 3.1

Auxiliary raster grid creation and edge detection on spectrogram

In order to track frequency ridges, the same image preparation method can be used as for evaluating medical diagnostic Moiré images. The tracking of frequency components is feasible by averaging the results of rising and falling edge detection on a created auxiliary raster grid on a greyscale STFT power spectra spectrogram derived from vibration signals of rotating machines.

Related publications: [MG1, MG2, MG3, MG4, MG5, MG6, MG7]

Thesis 3.2

Frequency component tracking on the image

The Differential and the Moving-Average-Predictive Tracking Methods - which have the same initial and end conditions but their core are mathematically different - can track frequency ridges on a greyscale STFT power spectra spectrogram derived from vibration signals of rotating machines.

Differential Tracking Method

The basics of the differential algorithm, which can track frequency ridges on a greyscale STFT power spectra spectrogram derived from vibration signals of rotating machines, are described by the following equations. The algorithm calculates the absolute vertical distance between the starting point and the detected points on the following line of the auxiliary grid as

$$\mathbf{d}_n = y_{i+1,n} - y_{i,j}, \tag{4.16}$$

where $\mathbf{d}$ is the vector of the calculated vertical differences, $y_{i+1,n}$ is the y coordinate of an intersection point on the $i+1$ vertical grid line and n is a running index which iterates over the elements of j. From the calculated differences the algorithm chooses the minimum absolute value and performs further examination on the detected $P_{i+1,j}$ point (in Eq. 4.17).

$$P_{i+1,j}(x_{i+1,j}; y_{i+1,j}), \tag{4.17}$$

where

$$x_{i+1} = x_i + \Delta_{mesh}, \tag{4.18}$$

$$y_{i+1,j} = y_{i,j} + \min|\mathbf{d}| \quad \text{if} \quad \min|\mathbf{d}| \leq \varepsilon \tag{4.19}$$

or

$$y_{i+1,j} = y_{i,j} \quad \text{if} \quad \min|\mathbf{d}| > \varepsilon, \tag{4.20}$$

where $P_{i+1,j}$ is the closest point based on differences; Δ_{mesh} is the difference between two vertical mesh lines; $\min|\mathbf{d}|$ is the minimum absolute value in the $\mathbf{d}$ vector and ε is the tolerance in pixels. If all of the differences in the collected vector are outside of the ε range the algorithm jumps to the next i vertical line. As the result of the tracking algorithm the found frequency components are collected into an $\mathbf{f}_k$ vector.

Related publications: [MG1, MG3, MG4]

Moving-Average-Predictive Tracking Method

The Moving-Average-Predictive Tracking Method estimates vertically where the next point of the actual frequency component has to be located on the following grid line and takes it as the initial point of the logic.

$$\tilde{P}_i(\tilde{x}_i; \tilde{y}_i), \tag{4.21}$$

where

$$\tilde{x}_i = x_{i,j}, \tag{4.22}$$

$$\tilde{y}_i = y_{i,j} + \tilde{\delta} \tag{4.23}$$

where $\tilde{\delta}$ is a predictor value, calculated by

$$\tilde{\delta} = \frac{\sum_{n=0}^{i} \mathbf{D}_n}{\dim(\mathbf{D})}, \tag{4.24}$$

where

$$\mathbf{D}_i = \min |\mathbf{d}|, \tag{4.25}$$

$$\tilde{\mathbf{d}}_n = y_{i+1,n} - \tilde{y}_i, \tag{4.26}$$

where $\mathbf{D}$ is the collected minimum absolute difference values along with the points of a found, complete frequency component.

Then the algorithm performs further examination on the detected $P_{i+1,j}$ point (in Eq. 4.27).

$$P_{i+1,j}(x_{i+1,j}; y_{i+1,j}), \tag{4.27}$$

where

$$x_{i+1} = x_i + \Delta_{mesh}, \tag{4.28}$$

$$y_{i+1,j} = \tilde{y}_i + \min |\tilde{\mathbf{d}}| \quad \text{if} \quad \min |\tilde{\mathbf{d}}| \leq \varepsilon \tag{4.29}$$

or

$$y_{i+1,j} = y_{i,j} \quad \text{if} \quad \min |\tilde{\mathbf{d}}| > \varepsilon, \tag{4.30}$$

where $P_{i+1,j}$ is the closest point based on differences between the predicted point and the found points; $\min|\tilde{\mathbf{d}}|$ is the minimum absolute value in the $\mathbf{d}$ vector and ε is the tolerance in pixels. If all of the differences in the collected vector are outside of the ε range the algorithm jumps to the next i vertical line.

Related publications: [MG1, MG3, MG4]

Thesis 3.3

Image to TF transformation

The frequency ridges, found after the execution of the component tracking algorithms on a greyscale STFT power spectra spectrogram derived from vibration signals of rotating machines, can be transferred back from the image to the time-frequency domain using the following parameters of the spectrogram image creation:

(a) Image resolution in pixels

(b) Frequency resolution in pixels

(c) Resolution in pixels

Related publications: [MG1, MG3, MG4]

Chapter 5

Validation and Verification of the Hybrid Method

The main content of Chapter 5 is based on publications [11, 116–120].

5.1 Developed Software Application

During the development of such an expert system, it was essential to look after the scalability and the maintainability besides resource requirements. In order to meet these primary conditions, a software package was developed within NI LabVIEW 2014 programming environment. LabVIEW was chosen because it is a traceable, modular graphical programming language, and its Sound and Vibration toolkit has several functions which could ease the development process.

The developed program, which block diagram can be seen in Fig. 5.1, had two main modules: data acquisition and data analysis related to the data analysing module, it was possible to load, analyse measured signals and export results generated by vibration diagnostic methods. The methods implemented in the software will be presented in the next section. The software was developed based on modular and scalable way that facilitates integrating new methods.

The measurements could be performed by as many channels as the data acquisition card could accept. According to this, it is able to select the desired channel(s) of the measured signal wanted to be loaded. The loaded signal was stored in the background; therefore,

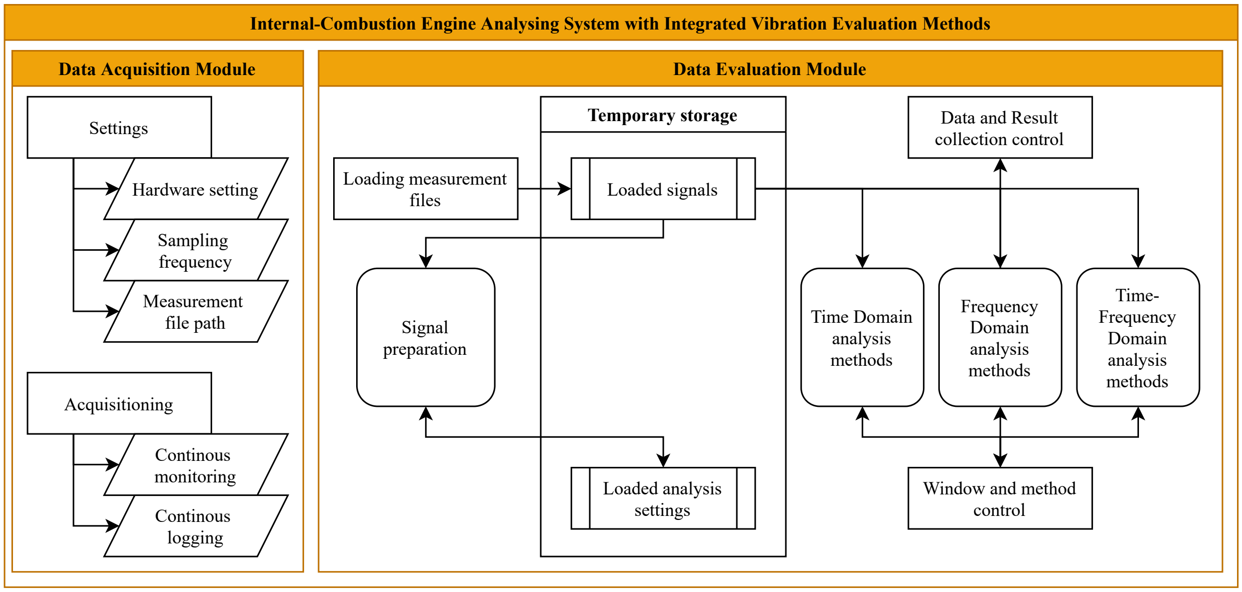

Figure 5.1: Software block diagram

several signals could be loaded parallel.

It is cardinal in terms of the data management of the analysing algorithms to share the time signal and its spectra. To make sure that the computer's memory will not be overloaded and the calculations of the methods are not time consuming, dynamic data sharing has been implemented. The system stored and managed the loaded measured signals to be analysed in a central database free to access all diagnostic algorithms. After preparing a signal (or spectra), the system copied it to another database that contained the analyse-ready signals. The sharing between the algorithms could be done manually or automatically. The diagnostic methods could be operated in parallel because of the window management of the system (every method had a separate window). To export the results of the methods, an exporting control software has been developed. This checks which method's window is opened, and its results will be saved into the desired file format (one or more extension could be selected too). All saved files contained the current date and the identifier of the measured signal. It can be selected whether only the results should be saved or the graphs and their data during the process. Besides the results, the input parameters of the algorithms will be saved into the file in all cases.

To make it possible to analyse ICE 's vibration components, mathematical vibration diagnostic methods were tested. These methods made it possible (after the preparation of the measured signal) to calculate such numerical indicators which could give information about the engine's condition. A later research plan is to use these parameters to predict malfunctions.

5.2 Validation on the Simulated Signals

In order to complete the validation of the method, the evaluations shown in Fig. 5.2 and Fig. 5.3 were performed. The results show that the method works appropriately when the rotating frequency changes rapidly. In terms of further results, it can be stated that the system can track and determine the transient frequency components, without increasing the time of calculation, in signals with various SNR if SNR is higher than -23 dB. If SNR is lower, the components on the image will be so blurred that the evaluation will not be reliable. This threshold was determined by automatically distorting the greyscale spectrogram images of available, recorded signals on multiple rotating machines until the system could clearly distinguish the falling and rising edges. E.g. in Fig. 5.3c and Fig. 5.3e one detected ridge, and the related image-frequency ridge started to fluctuate slightly around 0.8 s. The reason is that the high background noise is contaminating the frequency ridge on the spectrogram in Fig. 5.3a at this time section. With decreased SNR value, this contamination will affect the evaluation more and more.

In literature, several ridge detection method can be found which process non-stationary signals and support fault diagnosis. Accordingly, at the end of this chapter, it can not be neglected to compare the introduced method briefly with some examples. References [121–123] discuss enhanced order based ridge detection where the basic vibration evaluation method is the STFT as well. In these studies, the complete method is performed in the TF domain, and cost function based decisions were inserted to identify the frequency ridges and detect malfunctions. In contrast, in our presented approach, ridge detection is performed in image space because amplitude information can be compressed by greyscale normalisation without losses to gain computational resources, and the method can also be customised on real-time systems. Tacholess solutions, presented in [124–126], are also suitable for ridge detections. These researches imply STFT and order-based representations and demodulation and resampling techniques for larger frequency ridge changes. Compared to these methods, the actually discussed approach in this thesis, does not require resampling or demodulation due to the intermediate image processing steps which operate with pixels. The presented ridge detection process is enhanced to find the frequency ridges of the complete constructions instead of focusing on one part of a rotating machine. Peeters et al. [127] investigates seven different instantaneous angular speed estimation methods, namely signal demodulation and tracking in a time-frequency representation of the signal. In comparison, the presented approach also has several parameters which have to be adjusted manually during analysis, but there is no clear information about the SNR limits with which the methods can operate reliably. In addition, in terms of speed, our method provides results around every 10 seconds and opens the possibility to deploy as a real-time application easier due to the image space analysis. This speed can be improved further by software engineering the image processing part without influencing the reliability of our method. This means that the two main parts of the method - signal processing and image processing - can be separated for optimisation independent of each other. As a disadvantage, it can be highlighted, compared to the studies mentioned above, that our proposed method is not adaptive at the moment, but in terms of further development, the algorithm's parameters could be fine-tuned automatically easily. In addition, the TF results obtained by the introduced image processing based method could be forwarded to those malfunction diagnosis methods, which were presented in many references in order to support condition monitoring.

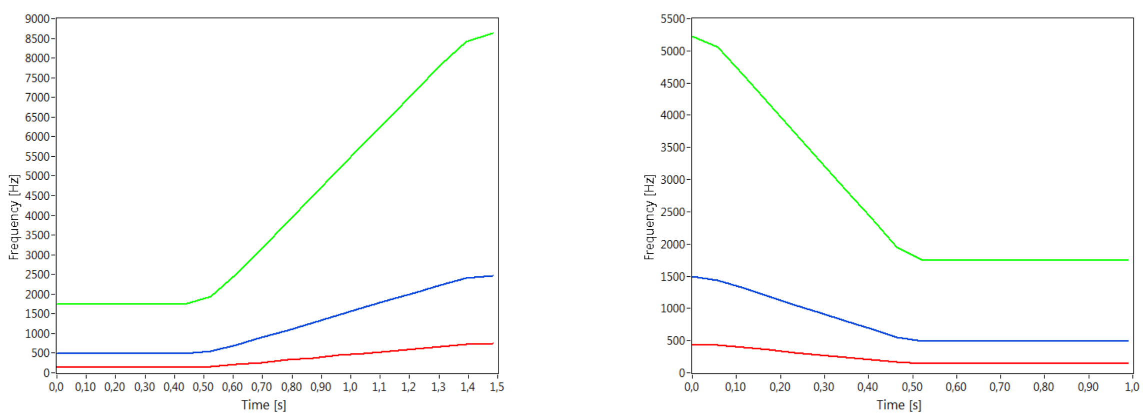

(a) Results of Setup 3 - high RPM gradient

(b) Results of Setup 4 - low RPM gradient

Figure 5.2: Evaluation results on simulated signals with different RPM gradient introduced in Table 2.3

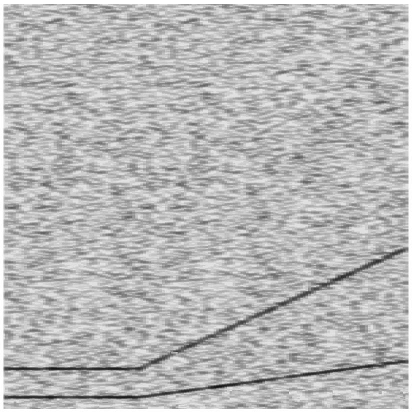

(a) Greyscale TFD image of Setup 5 - low SNR

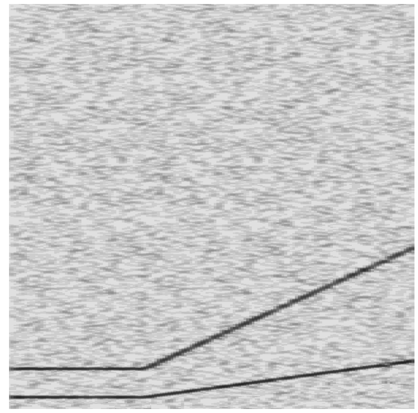

(b) Greyscale TFD of Setup 6 - high SNR

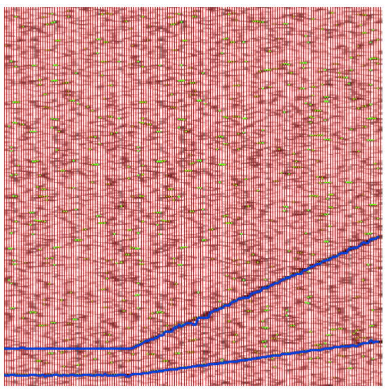

(c) Evaluated image of Setup 5 - low SNR

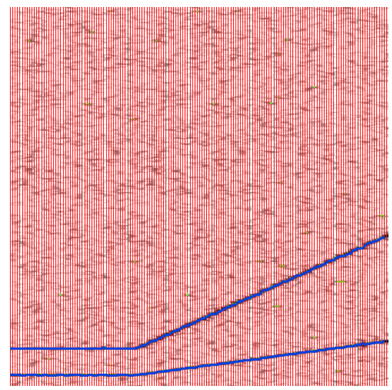

(d) Evaluated image of Setup 6 - high SNR

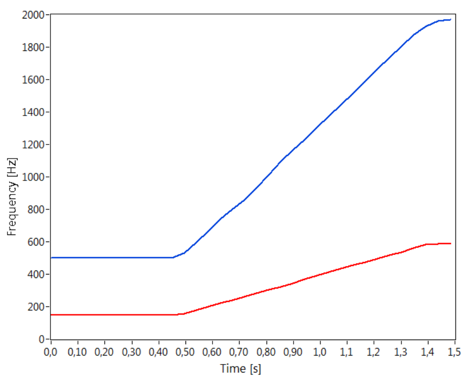

(e) Results of Setup 5 - low SNR

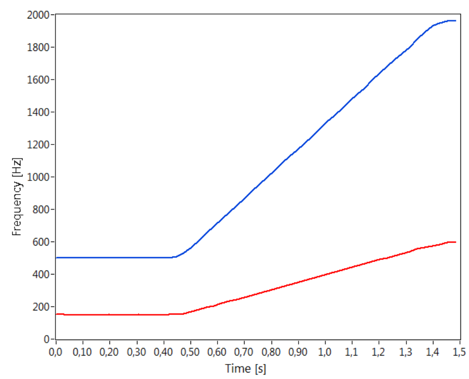

(f) Results of Setup 6 - high SNR

Figure 5.3: Evaluation results on simulated signals with different SNR ratio introduced in Table 2.4 (colours in the greyscale image: red - vertical mesh lines, black - frequency components, blue - result of the component tracking).

5.3 Method Verification

During the validation part of the research, real measurement evaluation results were captured as well in order to test and validate the created method on an existing rotating machine construction. This evaluation aims to check the operation of the method and observe what sort of frequency component information can be obtained.

The created analysing method will be demonstrated on an ICE measurement, and its details are summarised in Table 5.1. During these measurements, physical quantities such as vibration, speed of rotation are recorded with the mentioned standard industrial knock sensor. During the test of the method on a real application, a 3.0L V6 diesel engine was mounted on a dynamometer. This engine type is a commonly used construction in passenger cars on the market. The measurement system represented in Fig. 5.4 contains the dynamometer, dynamometer control and fuel consumption measurement. The fuel consumption measurement system itself controlled fuel temperature. In parallel, the intake air has been temperature-controlled as well in order to be able to repeat the same mass related air to fuel in-cylinder parameters.

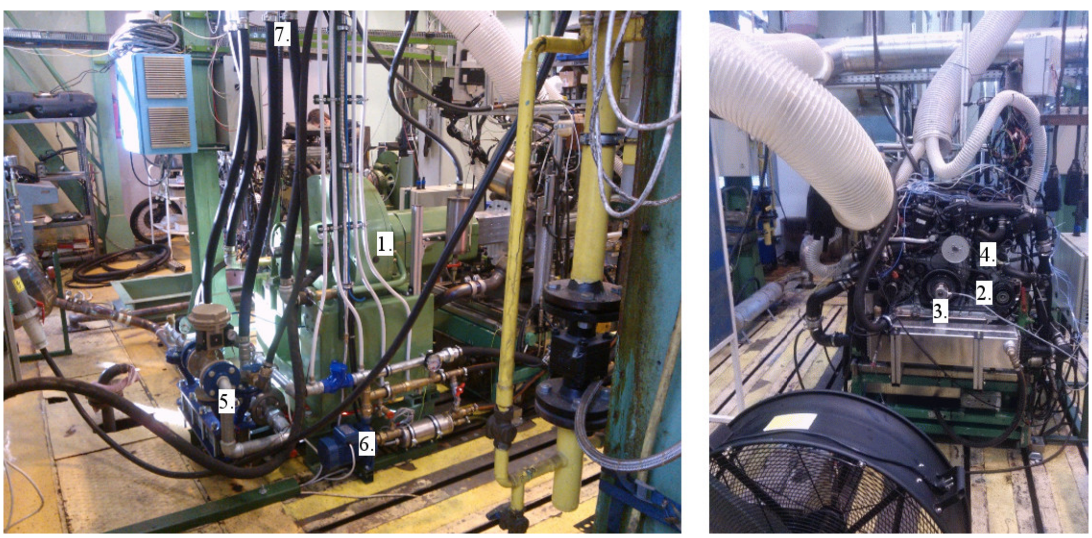

Figure 5.4: The test rig used for validation (1 - Dynamometer, 2 - 3.0 V6 Diesel engine, 3 - Mounted encoder, 4 - Mounting position of the knock sensor, 5 - KW system, 6 - Intercooler coolant heat exchanger, 7 - Cooling circuit connection)

Vibration measurement was carried out with a piezoelectric knock sensor (Siemens 07K-905-377-C, with 1-20 kHz measurement range and 35 ± 8 mV/g @ 5 kHz accuracy) attached to its designated location on construction. It is advantageous to use this sensor as it was mounted on the rotating machine during the manufacturing process, and the construction does not need to be disrupted. In a particular case, the outcome of this test can state that the analysis without mounting any additional vibration sensor on the construction can be performed. In order to acquire the speed of rotation information, an incremental optical encoder (Kübler 8.5802.2173.1024, with 0-12000 RPM range and 1024/RPM resolution) was attached to the crankshaft.

For data acquisition, via analogue and counter input, an NI USB-6361 was used. The analogue channel had a 16-bit resolution with a maximum 2 MS/s sampling frequency on a maximum ±10 V range. In addition, the counter channel has a 32-bit resolution with a maximum 100 MHz internal base clock. The measurement and complete analysis were performed with the above mentioned self-developed software package.

Table 5.1: Test measurement description for method validation

Name	**Type**
DUT	3.0 V6 Diesel engine
Dynamometer	Eddy-current; Borghi & Saveri FE-350S
Fuel consumption meas. system	AVL-7030 Fuel Balance
Physical quantities	Axial vibration, Crankshaft speed
Used sensor type	Knock sensor, Encoder
Derived quantities	Vibration, Revolution
Measured transient behaviour	Mixed states (Ramp-down section from 4200 RPM to 2000 RPM and a constant section)

The measurement was defined to record the axial vibration signal of the engine and the crankshaft speed as a reference during a deceleration phase from 4200 RPM to 2000 RPM. After reaching steady-state, a constant 2000 RPM section was recorded as well. The dynamometer was externally controlled to ensure that the gradient of the rotating speed and the gradient of the torque is constant during the time. This definition guaranteed that the measured signal for validation will contain different gradient states and steady-state as well in order to study the operation of the method.

The intention was to track transient frequency components on the spectrogram image in various operational conditions with the proposed method using an industrial knock sensor. During the signal analysis, the signal and image processing methods had the following parameters. In order to produce the spectrogram, after applying a low-pass filter for the

0-1 kHz range, a 2.8 s long transient signal section was cut out. The STFT was performed using a 0.15 s Hanning-window with 0.03 s sliding based on a 30000 point DFT calculation. The application of these parameters produced a maximal 1.26 Hz frequency resolution and 0.004 s time resolution. In the case of internal combustion engines, it is adequate because ECU's crankshaft revolution control always has an inaccuracy around $\pm 3 - 5$ % RPM. The analysis in the mentioned frequency range is optimal because the bandwidth of the sensor and the mechanical conditions of the construction can be observed in this range.

In spectrogram image evaluation, it is always necessary to improve the quality of the image to ensure the reliable the detection of white-black transitions. To accomplish this, after performing an image cut action to eliminate the frequency suppression section generated by the low-pass filter, BCG correction using parameters $B = 171, C = 56, G = 1.51$ was applied. It was followed by a histogram correction and a convolutional 6×6 Gaussian filter with additional low-pass image filtering to get the best separation of the edges of the frequency components in the greyscale image. These steps and parameters are in accordance with the parameters used for the simulated signal evaluation in section 3.4 and section 3.3. The intersection point detection of the image evaluation was carried out based on the averaging method with a 5-pixel resolution of the vertical auxiliary grid lines followed by the MAPTM component tracking method. Following the back-transformation of the detected frequency components into the TF domain, smoothing was performed with the point-by-point windowing based on the same parameters presented in section 4.2 to obtain more reliably the constant and variable parts of the signal.

The summarised results of the analysis are presented in Fig. 5.5. The images demonstrate each step of the evaluation method. Furthermore, Fig. 5.5a demonstrates that how the ICE engine control unit (ECU) performs the stepwise control from 4200 RPM to the 2000 RPM steady-state. The method can track the components between ramped and constant states with high reliability in the highlighted frequency range. This can be stated based on Fig. 5.5b. Although few false detections appear, those tracked lines will be eliminated based on the end line criteria presented in section 4.2. The raw, tracked frequency component ridges presented in Fig. 5.5c show that the detected frequency lines do not have a constant slope due to the stepwise RPM control of the machine. This means that the presented hybrid method can detect the frequency components on the spectrogram image independently from the rate of change of the RPM. By executing the frequency line smoothing as the final step, the

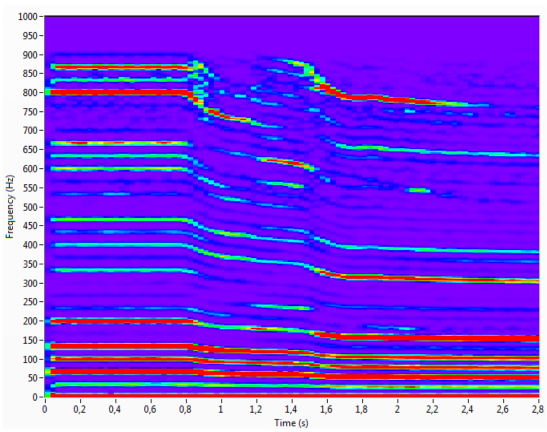

(a) The generated spectrogram from the signal

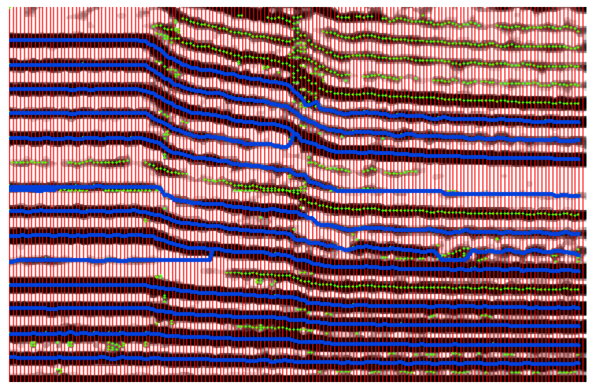

(b) MAP component tracking algorithm execution

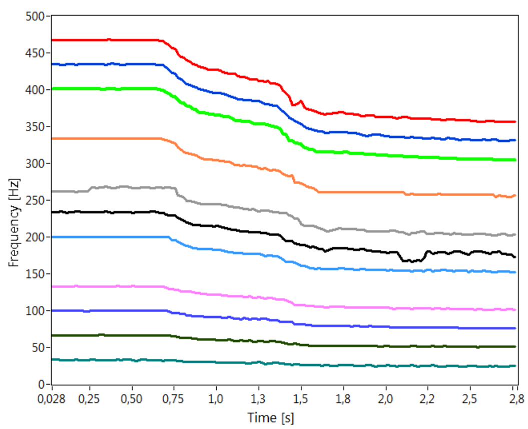

(c) Raw results transferred back to TF domain

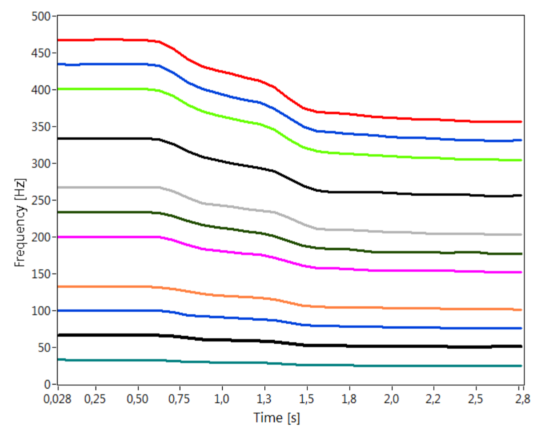

(d) Final results after smoothing algorithm

Figure 5.5: Results of the evaluation method carried out on a real diesel engine operating in transient states

final results (Fig. 5.5d) in the TF domain were achieved. This data can be used for further analysis in order to extract outcomes on the condition of the rotating parts in the machine. In Fig. 5.5a, the harmonics in the TF domain can be observed clearly, and the diagnosis result can be directly concluded by combining the structure parameters of the drivetrain. Therefore, it is not necessary to extract the image-frequency ridges in this case, but the importance of this setup was to demonstrate and validate the operation of the method on a real rotating machine. Difficulty might arise when the extracted instantaneous frequency ridges are background noises and not fundamental harmonics. This method was prepared for industrial application and assumed that basic structural information about the rotating machine is available. Thus, detected noise and actual harmonic ridges are separable based on the details of the mechanical construction.

5.4 Novel Results

In this section those novel results will be summarized which are related to the part of the research work presented in Chapter 5.

5.4.1 Thesis Group 4.

The following thesis are mainly grouped around the application of the method. The verification showed that the hybrid method can be applied to the following cases.

Thesis 4.1

Frequency component tracking

Rotating machine transient frequency components can be detected independently of their gradient by evaluating a greyscale STFT spectrogram image using image processing and tracking methods in case of vibration signals with SNR value higher than -23 dB.

Related publications: [MG1]

Thesis 4.2

Dedicated frequency component determination

Selected rotating machine frequency component can be detected indirectly using image processing methods by evaluating the power spectra spectrogram as a greyscale image, resulting from the STFT method used in vibration diagnostics.

Related publications: [MG1, MG3, MG4]

Thesis 4.3

Parameter optimization possibilities for different types of rotary machines

The complete process, which is capable of tracking frequency components using image processing methods by evaluating the power spectra spectrogram as a greyscale image, can be optimised for different types of rotating machines. This optimization can be performed using a custom-developed software package with the fine-tuning of the parameters of the method steps which are

(a) sampling frequency,

(b) time resolution of the Short-Time Fourier Transform,

(c) frequency resolution of the Short-Time Fourier Transform,

(d) Fourier Transform window width and overlapping,

(e) image resolution,

(f) Brightness-Contrast-Gamma correction values,

(g) auxiliary raster grid resolution,

(h) edge detection pixel threshold,

(i) tracking algorithm type,

(j) tracking algorithm tolerance.

Related publications: [MG1, MG2, MG8, MG9, MG10]

Chapter 6

Future Improvements

The method presented in this thesis served the purpose of highlighting several disciplines that can help each other to solve a given problem. As a result, there might be various opportunities in order to improve the process.

In terms of further development, first of all, during STFT creation the Variable Frequency Resolution Short-Time Fourier Transformation (VFR-STFT) represented in [128, 129], could be introduced with which the frequency and time resolution of the STFT could be manipulated along one Fourier-transformation as well.

As the complete method was built up by using well-defined steps, an automation process could be tailored to dynamically evaluate measurements right after acquisition. Starting with the STFT creation, parameters could be fine-tuned automatically because the sampling frequency and the length of the relevant signal section is known. Additionally, the windowing parameters could be adjusted based on these information which could result in a better, cleaner spectrogram.

Image export could be emphasised as well by automatic greyscale export and with variable resolution options. This solution could highlight those parts of the spectrogram which contain interesting sections. This step could be supplemented by a spectrogram versus image resolution benchmark.

In case of image preparation the BCG parameters could be dynamically changed using image vectors or matrices as the function of the original STFT amplitude values. The mesh generation could be executed automatically by setting the density based on the time resolution of the spectrogram. The component tracking algorithms could also provide better results if the resolution of the auxiliary mesh and the tolerance value would be varied as the function of the sampling frequency and the original STFT frequency resolution. Moreover, the tracking algorithm parameters could be fine-tuned using neural networks or other deep learning algorithms if several measurement would be available.

Last, but not least the complete method could be reworked on code level in a way to make it possible for real-time data processing because the evaluation of a section could be paralleled and the spectrogram creation and image processing is a bit-wise operation. Meeting these challenges will pave the way towards the deployment of the complete method in real-time or Field-Programmable Gate Array (FPGA) environment in industrial applications for condition monitoring purposes.

Bibliography

[1] Jyoti Kumar Sinha. *Vibration Analysis, Instruments, and Signal Processing.* CRC Press, December 2014.

[2] S. Nandi, H.A. Toliyat, and X. Li. Condition Monitoring and Fault Diagnosis of Electrical Motors—A Review. *IEEE Transactions on Energy Conversion*, 20(4):719–729, December 2005.

[3] Ling Wang, Jian Chu, and Jun Wu. Selection of optimum maintenance strategies based on a fuzzy analytic hierarchy process. *International Journal of Production Economics*, 107(1):151–163, May 2007.

[4] Horst Kuemmlee, Thomas Gross, and Josef Kolerus. Machine vibrations and diagnostics the world of ISO. In *Industry Applications Society 60th Annual Petroleum and Chemical Industry Conference*, pages 1–13, September 2013.

[5] Dale Hoiberg. *Encyclopedia Britannica.* Encyclopædia Britannica Inc., 15 edition, 2009.

[6] Isabela F. Apolinário and Paulo S. R. Diniz. Chapter 1 - Introduction to Signal Processing Theory. In Paulo S. R. Diniz, Johan A. K. Suykens, Rama Chellappa, and Sergios Theodoridis, editors, *Academic Press Library in Signal Processing*, volume 1 of *Academic Press Library in Signal Processing: Volume 1*, pages 3–28. Elsevier, January 2014.

[7] Asoke Nandi and Hosameldin Ahmed. *Condition Monitoring with Vibration Signals: Compressive Sampling and Learning Algorithms for Rotating Machine.* Wiley, 1 edition, December 2019.

[8] Gábor Manhertz, Gábor Gárdonyi, and Gábor Pór. Managing measured vibration data for malfunction detection of an assembled mechanical coupling. *The International Journal of Advanced Manufacturing Technology*, 75(5):693–703, 2014.

[9] Gábor Gárdonyi and Gábor Manhertz. Rezgésdiagnosztikai Algoritmusok Fejlesztése Elektromotoros Hajtásrendszer Vizsgálatához. In *Tavaszi Szél 2013 / Spring Wind 2013*, volume I, pages 169–178, 2013.

[10] A. Wald. Sequential Tests of Statistical Hypotheses. *The Annals of Mathematical Statistics*, 16(2):117–186, 1945. Publisher: Institute of Mathematical Statistics.

[11] Gábor Manhertz and Ákos Bereczky. Development of a vibration expert system to analyze and predict malfunctions in internal-combustion engine. In *Proceedings of ARES '14*, pages 24–29, 2014.

[12] Digital Signal Processing: System Analysis and Design (2010), August 2010.

[13] Charles Van Loan. *Computational frameworks for the fast Fourier transform.* Society for Industrial and Applied Mathematics, USA, 1992.

[14] S Edwards, Arthur W Lees, and Michael I Friswell. Fault Diagnosis of Rotating Machinery. *The Shock and Vibration Digest*, 30(1):4–13, 1998.

[15] Basim Al-Najjar. Total quality maintenance: An approach for continuous reduction in costs of quality products. *Journal of Quality in Maintenance Engineering*, 2(3):4–20, January 1996.

[16] D. Shi, D. A. Axinte, and N. N. Gindy. Development of an online machining process monitoring system: a case study of the broaching process. *The International Journal of Advanced Manufacturing Technology*, 34(1):34–46, August 2007.

[17] Rajesh Ganesan. Real-time monitoring of complex sensor data using wavelet-based multiresolution analysis. *The International Journal of Advanced Manufacturing Technology*, 39(5):543–558, November 2008.

[18] Jiujun Zhang, Zhonghua Li, and Zhaojun Wang. A new adaptive control chart for monitoring process mean and variability. *The International Journal of Advanced Manufacturing Technology*, 60(9):1031–1038, June 2012.

[19] Chris K. Mechefske and Qiao Sun. Failure detection in automotive light assemblies during vibration endurance testing. *The International Journal of Advanced Manufacturing Technology*, 51(5):799–810, November 2010.

[20] Wei Hu, Qiao Sun, and Chris K. Mechefske. Condition monitoring for the endurance test of automotive light assemblies. *The International Journal of Advanced Manufacturing Technology*, 66(5):1087–1095, May 2013.

[21] M. B. Walter. Mechanical diagnostics-past, present and future. In *IEEE Conference on Systems Readiness Technology, 'Advancing Mission Accomplishment'.*, pages 517–521, September 1990.

[22] A. H. Rawicz and H. X. Jiang. Diagnostic expert-system for mechanical reliability in heavy trucks. In *Annual Reliability and Maintainability Symposium 1992 Proceedings*, pages 426–431, January 1992.

[23] Csaba Budai and László L. Kovács. Friction Effects on Stability of a Digitally Controlled Pendulum. *Periodica Polytechnica Mechanical Engineering*, 59(4):176–181, October 2015.

[24] Csaba Budai and László L. Kovács. On the Stability of Digital Position Control with Viscous Damping and Coulomb Friction. *Periodica Polytechnica Mechanical Engineering*, 61(4):266–271, September 2017.

[25] Csaba Budai, László L. Kovács, József Kövecses, and Gábor Stépán. Effect of dry friction on vibrations of sampled-data mechatronic systems. *Nonlinear Dynamics*, 88(1):349–361, April 2017.

[26] Csaba Budai, László L. Kovács, and József Kövecses. Analysis of the Effect of Coulomb Friction on Haptic Systems Dynamics. American Society of Mechanical Engineers Digital Collection, December 2016.

[27] Csaba Budai, László L. Kovács, and József Kövecses. Combined Effect of Sampling and Coulomb Friction on Haptic Systems Dynamics. *Journal of Computational and Nonlinear Dynamics*, 13(6), June 2018. Publisher: American Society of Mechanical Engineers Digital Collection.

[28] Csaba Budai, László L. Kovács, József Kövecses, and Gábor Stépán. Combined effects of sampling and dry friction on position control. *Nonlinear Dynamics*, 98(4):3001–3007, December 2019.

[29] Stephan Ebersbach and Zhongxiao Peng. Expert system development for vibration analysis in machine condition monitoring. *Expert Systems with Applications*, 34(1):291–299, January 2008.

[30] Hirpa L. Gelgele and Kesheng Wang. An expert system for engine fault diagnosis: development and application. *Journal of Intelligent Manufacturing*, 9(6):539–545, December 1998.

[31] X. Song, X. Li, W. Zhang, and W. Zhou. The new measurement algorithm of the engine speed base on the basic frequency of vibration signal. In *2010 International Conference on Computer, Mechatronics, Control and Electronic Engineering*, volume 5, pages 273–277, August 2010.

[32] Shengchun Wang, Shijun Song, Tonghong Jin, and Xiaowei Wang. Adaptive Chirplet Decomposition Method and Its Application in Machine Fault Diagnosis. In *2009 2nd International Congress on Image and Signal Processing*, pages 1–5, October 2009.

[33] Jian-Da Wu, Mingsian R. Bai, Fu-Cheng Su, and Chin-Wei Huang. An expert system for the diagnosis of faults in rotating machinery using adaptive order-tracking algorithm. *Expert Systems with Applications*, 36(3, Part 1):5424–5431, April 2009.

[34] Siliang Lu, Qingbo He, and Jun Wang. A review of stochastic resonance in rotating machine fault detection. *Mechanical Systems and Signal Processing*, 116:230–260, February 2019.

[35] Darian M. Onchis, Ruqiang Yan, and Pavel Rajmic. Time–frequency methods for condition based maintenance and modal analysis. *Signal Processing*, 96, March 2014.

[36] Gábor Gárdonyi and Krisztián Samu. Hybrid spectral speed determination method for rotary machines. *Journal of Vibroengineering*, 21(3):538–555, 2019.

[37] Gábor Gárdonyi and Krisztián Samu. Comparison of Vibration Spectra and Cepstra used for Determining the Rotational Speed of Rotary Machines. In *Proceedings of CERIS '14*, 2014.

[38] Gábor Gárdonyi and Krisztián Samu. Spectrum and Cepstrum Based Speed Determination of Stepper Motors. In *2018 IEEE 18th International Power Electronics and Motion Control Conference (PEMC)*, pages 870–877, August 2018. ISSN: 2473-0165.

[39] Hojjat Ahmadi and Zeinab Khaksar. Power Spectral Density Technique for Fault Diagnosis of an Electromotor. In Estevam Rafael Hruschka, Junzo Watada, and Maria do Carmo Nicoletti, editors, *Integrated Computing Technology*, Communications in Computer and Information Science, pages 105–112, Berlin, Heidelberg, 2011. Springer.

[40] Daming Lin, Murray Wiseman, Dragan Banjevic, and Andrew K. S. Jardine. An approach to signal processing and condition-based maintenance for gearboxes subject to tooth failure. *Mechanical Systems and Signal Processing*, 18(5):993–1007, September 2004.

[41] Xiang-Qun Liu, Hong-Yue Zhang, Jun Liu, and Jing Yang. Fault detection and diagnosis of permanent-magnet DC motor based on parameter estimation and neural network. *IEEE Transactions on Industrial Electronics*, 47(5):1021–1030, October 2000.

[42] Jian-Da Wu, Peng-Hsin Chiang, Yo-Wei Chang, and Yao-jung Shiao. An expert system for fault diagnosis in internal combustion engines using probability neural network. *Expert Systems with Applications*, 34(4):2704–2713, May 2008.

[43] Wenli Shang, Xiaofeng Zhou, and Jie Yuan. An intelligent fault diagnosis system for newly assembled transmission. *Expert Systems with Applications*, 41(9):4060–4072, July 2014.

[44] Carlos López-Escobar, Rafael González-Palma, David Almorza, Pedro Mayorga, and María Carmen Carnero. Statistical quality control through process self-induced vibration spectrum analysis. *The International Journal of Advanced Manufacturing Technology*, 58(9):1243–1259, February 2012.

[45] Jose Vicente Abellan-Nebot and Fernando Romero Subirón. A review of machining monitoring systems based on artificial intelligence process models. *The International Journal of Advanced Manufacturing Technology*, 47(1):237–257, March 2010.

[46] Gang Yu, Changning Li, and Jun Sun. Machine fault diagnosis based on Gaussian mixture model and its application. *The International Journal of Advanced Manufacturing Technology*, 48(1):205–212, April 2010.

[47] Chih-Cherng Chen, Nun-Ming Liu, Ko-Ta Chiang, and Hua-Lun Chen. Experimental investigation of tool vibration and surface roughness in the precision end-milling process

using the singular spectrum analysis. *The International Journal of Advanced Manufacturing Technology*, 63(5):797–815, November 2012.

[48] Tien-I Liu, Junyi Lee, Palvinder Singh, and George Liu. Real-time recognition of ball bearing states for the enhancement of precision, quality, efficiency, safety, and automation of manufacturing. *The International Journal of Advanced Manufacturing Technology*, 71(5):809–816, March 2014.

[49] Morteza Ghobakhloo. The future of manufacturing industry: a strategic roadmap toward Industry 4.0. *Journal of Manufacturing Technology Management*, 29(6):910–936, January 2018.

[50] Hardik Majiwala, Pankaj Gandhi, and Parag Sanghani. Development of Decision Support System (DSS) Framework for Predictive Maintenance of Rolling Element Bearing in the Emerging Era of Industry 4.0. SSRN Scholarly Paper ID 3167428, Social Science Research Network, Rochester, NY, April 2018.

[51] Diego D'Urso, Ferdinando Chiacchio, Dario Borrometi, Antonio Costa, and Lucio Compagno. Dynamic failure rate model of an electric motor comparing the Military Standard and Svenska Kullagerfabriken (SKF) methods. *Procedia Computer Science*, 180:456–465, January 2021.

[52] Changting Wang and R. X. Gao. Wavelet transform with spectral post-processing for enhanced feature extraction [machine condition monitoring]. *IEEE Transactions on Instrumentation and Measurement*, 52(4):1296–1301, August 2003.

[53] W.-X. Yang and X.-M. Ren. Detecting Impulses in Mechanical Signals by Wavelets. *EURASIP Journal on Advances in Signal Processing*, 2004(8):946162, December 2004.

[54] Ruqiang Yan, Robert X. Gao, and Xuefeng Chen. Wavelets for fault diagnosis of rotary machines: A review with applications. *Signal Processing*, 96:1–15, March 2014.

[55] Richard A. Altes. Detection, estimation, and classification with spectrograms. *The Journal of the Acoustical Society of America*, 67(4):1232–1246, April 1980.

[56] Aled T. Catherall and Duncan P. Williams. High resolution spectrograms using a component optimized short-term fractional Fourier transform. *Signal Processing*, 90(5):1591–1596, May 2010.

[57] Vladimir Dekys, Peter Kalman, Pavel Hanak, Pavol Novak, and Zuzana Stankovicova. Determination of Vibration Sources by Using STFT. *Procedia Engineering*, 177:496–501, January 2017.

[58] Ahmad Taghizadeh-Alisaraei and Alireza Mahdavian. Fault detection of injectors in diesel engines using vibration time-frequency analysis. *Applied Acoustics*, 143:48–58, January 2019.

[59] G. Akti and D. Goularas. Frequency component extraction from color images for specific sound transformation and analysis. In *2012 3rd International Conference on Image Processing Theory, Tools and Applications (IPTA)*, pages 253–258, October 2012.

[60] J. Zhang, W. Lin, K. M. Jacobs, and X. Hu. Extraction of microsphere size from diffraction images with an STFT method. In *2012 IEEE International Conference on Virtual Environments Human-Computer Interfaces and Measurement Systems (VECIMS) Proceedings*, pages 213–216, July 2012.

[61] D. Van Cappel and P. Alinat. Frequency line extractor using multiple hidden Markov models. In *IEEE Oceanic Engineering Society. OCEANS'98. Conference Proceedings (Cat. No.98CH36259)*, volume 3, pages 1481–1485 vol.3, September 1998.

[62] J. S. Abel, H. J. Lee, and A. P. Lowell. An image processing approach to frequency tracking (application to sonar data). In *[Proceedings] ICASSP-92: 1992 IEEE International Conference on Acoustics, Speech, and Signal Processing*, volume 2, pages 561–564 vol.2, March 1992.

[63] Krzysztof Czarnecki. The instantaneous frequency rate spectrogram. *Mechanical Systems and Signal Processing*, 66-67:361–373, January 2016.

[64] Renata Klein, Eyal Masad, Eduard Rudyk, and Itai Winkler. Bearing diagnostics using image processing methods. *Mechanical Systems and Signal Processing*, 45(1):105–113, March 2014.

[65] Yu Zhang, Chris Bingham, Zhijing Yang, Bingo Wing-Kuen Ling, and Michael Gallimore. Machine fault detection by signal denoising—with application to industrial gas turbines. *Measurement*, 58:230–240, December 2014.

[66] Thierry Pun. A new method for grey-level picture thresholding using the entropy of the histogram. *Signal Processing*, 2(3):223–237, July 1980.

[67] P J Kootsookos. A Review of the Frequency Estimation and Tracking Problems. page 38, February 1999.

[68] Markos Markou and Sameer Singh. Novelty detection: a review—part 1: statistical approaches. *Signal Processing*, 83(12):2481–2497, December 2003.

[69] H. C. So. A comparative study of three recursive least-squares algorithms for single-tone frequency tracking. *Signal Processing*, 83(9):2059–2062, September 2003.

[70] Chuan Li, Vinicio Sanchez, Grover Zurita, Mariela Cerrada Lozada, and Diego Cabrera. Rolling element bearing defect detection using the generalized synchrosqueezing transform guided by time–frequency ridge enhancement. *ISA Transactions*, 60:274–284, January 2016.

[71] Thomas A. Lampert and Simon E. M. O'Keefe. On the detection of tracks in spectrogram images. *Pattern Recognition*, 46(5):1396–1408, May 2013.

[72] S. Pei and S. Huang. STFT With Adaptive Window Width Based on the Chirp Rate. *IEEE Transactions on Signal Processing*, 60(8):4065–4080, August 2012.

[73] L. Rankine, M. Mesbah, and B. Boashash. IF estimation for multicomponent signals using image processing techniques in the time–frequency domain. *Signal Processing*, 87(6):1234–1250, June 2007.

[74] F. J. Harris. On the use of windows for harmonic analysis with the discrete Fourier transform. *Proceedings of the IEEE*, 66(1):51–83, January 1978.

[75] Lennart Ljung and Keith Glover. Frequency Domain versus Time Domain Methods in System Identification: A Brief Discussion. *IFAC Proceedings Volumes*, 12(8):1309–1322, September 1979.

[76] G. M. Blair. A review of the discrete Fourier transform. 1. Manipulating the powers of two. *Electronics Communication Engineering Journal*, 7(4):169–177, August 1995.

[77] M.-C. Pan, P. Sas, and H. van Brussel. Nonstationary time-frequency analysis for machine condition monitoring. In *Proceedings of Third International Symposium on Time-Frequency and Time-Scale Analysis (TFTS-96)*, pages 477–480, June 1996.

[78] Michael Cerna and Audrey F Harvey. The Fundamentals of FFT-Based Signal Analysis and Measurement. 2000.

[79] S. A. Neild, P. D. McFadden, and M. S. Williams. A review of time-frequency methods for structural vibration analysis. *Engineering Structures*, 25(6):713–728, May 2003.

[80] Nagy István, Baksai Gábor, and Sólyomvári Károly. *Műszaki diagnosztika: állapotfüggő karbantartás*. Delta-3N, Paks, 2006. OCLC: 909517992.

[81] R.X. Gao and R. Yan. Non-stationary signal processing for bearing health monitoring. *International Journal of Manufacturing Research*, 1(1):18, 2006.

[82] Kenneth V Cartwright. Determining the Effective or RMS Voltage of Various Waveforms Without Calculus. *The Technology Interface*, page 20, 2007.

[83] Ervin Sejdić, Igor Djurović, and Jin Jiang. Time–frequency feature representation using energy concentration: An overview of recent advances. *Digital Signal Processing*, 19(1):153–183, January 2009.

[84] Manish Vishwakarma, Rajesh Purohit, V. Harshlata, and P. Rajput. Vibration Analysis & Condition Monitoring for Rotating Machines: A Review. *Materials Today: Proceedings*, 4(2, Part A):2659–2664, January 2017.

[85] Arun K M and Tc Manjunath. Vibration signal analysis using Time and Time frequency domain: Review. In *ICPCSI Proceedings*, Chennai, September 2017. ICPCSI.

[86] Wahyu Caesarendra and Tegoeh Tjahjowidodo. A Review of Feature Extraction Methods in Vibration-Based Condition Monitoring and Its Application for Degradation Trend Estimation of Low-Speed Slew Bearing. *Machines*, 5(4):21, December 2017.

[87] Cesar Da Costa. Review of Vibration Analysis Techniques.

[88] Elias Metsäntähti. Frequency Domain Methods in Diagnostics of Rotating Machines. page 90.

[89] Sidny Burrus, C. S. Burrus, Ramesh A. Gopinath, Haitao Guo, Jan E. Odegard, and Ivan W. Selesnick. *Introduction to Wavelets and Wavelet Transforms: A Primer*. Prentice Hall, 1998.

[90] I. Daubechies. The wavelet transform, time-frequency localization and signal analysis. *IEEE Transactions on Information Theory*, 36(5):961–1005, September 1990.

[91] O. Rioul and M. Vetterli. Wavelets and signal processing. *IEEE Signal Processing Magazine*, 8(4):14–38, October 1991.

[92] Shie Qian and Dapang Chen. Joint time-frequency analysis. *IEEE Signal Processing Magazine*, 16(2):52–67, March 1999.

[93] W. Y. Zhang, T. Hao, Y. Chang, and Y. H. Zhao. Time-frequency analysis of enhanced GPR detection of RF tagged buried plastic pipes. *NDT & E International*, 92:88–96, December 2017.

[94] Bo Li, Linqing Luo, Yifei Yu, Kenichi Soga, and Jize Yan. Dynamic Strain Measurement Using Small Gain Stimulated Brillouin Scattering in STFT-BOTDR. *IEEE Sensors Journal*, 17(9):2718–2724, May 2017.

[95] David Kleinfeld and Partha P. Mitra. Spectral Methods for Functional Brain Imaging. *Cold Spring Harbor Protocols*, 2014(3):pdb.top081075, March 2014.

[96] Petra Balla, Gábor Manhertz, and Ákos Antal. Diagnostic moiré image evaluation in spinal deformities. *OPTICA APPLICATA; 03/2016; ISSN 1429-7507*, 2016.

[97] K. Hane, Y. Uchida, and S. Hattori. Moiré displacement measurement technique for a linear encoder. *Optics & Laser Technology*, 17(2):89–95, April 1985.

[98] M. Batouche. A knowledge based system for diagnosing spinal deformations: moire pattern analysis and interpretation. In *11th IAPR International Conference on Pattern Recognition [1992] Proceedings*, pages 591–594, August 1992.

[99] Ming Wang. Fourier transform moiré tomography for high-sensitivity mapping asymmetric 3-D temperature field. *Optics & Laser Technology*, 34(8):679–685, November 2002.

[100] Emin Gabrielyan. The basics of line moire patterns and optical speedup. *arXiv:physics/0703098*, March 2007. arXiv: physics/0703098.

[101] Ming-Kuei Hu. Visual pattern recognition by moment invariants. *IRE Transactions on Information Theory*, 8(2):179–187, February 1962.

[102] M Sonka, V Hlavac, and R Boyle. *Image Processing, Analysis and Machine Vision*. Springer, 1993.

[103] J. C. Russ. *The Image Processing Handbook*. Springer, IEEE Press, 1999.

[104] J Berke, Gy Hegedűs, D Kelemen, and J Szabó. *Digitális képfeldolgozás és alkalmazásai*. V. E. Georgikon M. K, 2001.

[105] Willam K. Pratt. *Digital Image Processing*. John Wiley & Sons, Inc., 2007.

[106] P. S. Theocaris. *Moiré Fringes in Strain Analysis*. Pergamon Press, 1969.

[107] K. Patorski and M. Kujawinska. *Handbook of the Moire Fringe Technique - 1st Edition*. Elsevier, Amsterdam, 1993.

[108] F. Liu, J. Yang, and H. Yue. Moiré pattern removal from texture images via low-rank and sparse matrix decomposition. In *2015 Visual Communications and Image Processing (VCIP)*, pages 1–4, December 2015.

[109] Anne Holtsch, Tobias Euwens, Bernd Uder, Samuel Grandthyll, Frank Müller, and Uwe Hartmann. Analysis of atomic Moiré patterns on graphene/Rh(1 1 1). *Surface Science*, 668:107–111, February 2018.

[110] Gábor Fazekas. Onthe Coding of Digitized Pictures. *Periodica Polytechnica Transportation Engineering*, 19(1-2):41–47, 1991. Number: 1-2.

[111] László Czap. *Képfeldolgozás*. Miskolci Egyetem, 2010.

[112] Battista Biggio, Giorgio Fumera, Ignazio Pillai, and Fabio Roli. A survey and experimental evaluation of image spam filtering techniques. *Pattern Recognition Letters*, 32(10):1436–1446, July 2011.

[113] Ruchika Chandel and Gaurav Gupta. Image Filtering Algorithms and Techniques: A Review. *International Journal of Advanced Research in Computer Science and Software Engineering*, page 5, 2013.

[114] I. Pitas. State of the art of morphological and nonlinear digital image processing. In *IEE Colloquium on Morphological and Nonlinear Image Processing Techniques*, pages 1–4, June 1993.

[115] F. Russo. Image filtering based on piecewise linear models. In *2004 IEEE International Workshop on Imaging Systems and Techniques (IST) (IEEE Cat. No.04EX896)*, pages 7–12, May 2004.

[116] Gábor Manhertz, Dániel Modok, and Ákos Bereczky. Evaluation of short-time fourier-transformation spectrograms derived from the vibration measurement of internal-combustion engines. In *2016 IEEE International Power Electronics and Motion Control Conference (PEMC)*, pages 812–817, 2016.

[117] Gábor Manhertz, Dániel Modok, and Ákos Bereczky. Frekvenciakomponensek Követése Short-Time Fourier-Transzformáció Spektrogramon Képfeldolgozási Módszerekkel. In *Tavaszi Szél 2016 / Spring Wind 2016*, volume III, pages 239–250, 2016.

[118] Gábor Manhertz. Légfelesleg-tényező változásának hatása belsőégésű motor rezgésösszetevőire. In *Tavaszi Szél 2014 / Spring Wind 2014*, volume VII, pages 446–459, 2014.

[119] Gábor Manhertz and Ákos Antal. The effect of air-fuel equivalence ratio change on the vibration components of an internal-combustion engine. *Recent Innovations in Mechatronics*, 2(1-2):1–6, 2015.

[120] Gábor Gárdonyi, Gábor Manhertz, Ákos Antal, Ákos Bereczky, and Krisztián Samu. Belsőégésű Motor Üzemállapotának Jellemzésére Alkalmas Polárdiagramos Megjelenítési Módszerek. In *Tavaszi Szél 2015 / Spring Wind 2015*, volume III, pages 349–366, 2015.

[121] Tianyang Wang, Ming Liang, Jianyong Li, and Weidong Cheng. Rolling element bearing fault diagnosis via fault characteristic order (FCO) analysis. *Mechanical Systems and Signal Processing*, 45(1):139–153, March 2014.

[122] Yi Wang, Guanghua Xu, Qing Zhang, Dan Liu, and Kuosheng Jiang. Rotating speed isolation and its application to rolling element bearing fault diagnosis under large speed variation conditions. *Journal of Sound and Vibration*, 348:381–396, July 2015.

[123] Yi Wang, Peter W. Tse, Baoping Tang, Yi Qin, Lei Deng, Tao Huang, and Guanghua Xu. Order spectrogram visualization for rolling bearing fault detection under speed variation conditions. *Mechanical Systems and Signal Processing*, 122:580–596, May 2019.

[124] Ming Zhao, Jing Lin, Xiufeng Wang, Yaguo Lei, and Junyi Cao. A tacho-less order tracking technique for large speed variations. *Mechanical Systems and Signal Processing*, 40(1):76–90, October 2013.

[125] Ming Zhao, Jing Lin, Xiaoqiang Xu, and Yaguo Lei. Tacholess Envelope Order Analysis and Its Application to Fault Detection of Rolling Element Bearings with Varying Speeds. *Sensors*, 13(8):10856–10875, August 2013. Number: 8 Publisher: Multidisciplinary Digital Publishing Institute.

[126] Yi Wang, Guanghua Xu, Ailing Luo, Lin Liang, and Kuosheng Jiang. An online tacholess order tracking technique based on generalized demodulation for rolling bearing fault detection. *Journal of Sound and Vibration*, 367:233–249, April 2016.

[127] Cédric Peeters, Quentin Leclère, Jérôme Antoni, Peter Lindahl, John Donnal, Steven Leeb, and Jan Helsen. Review and comparison of tacholess instantaneous speed estimation methods on experimental vibration data. *Mechanical Systems and Signal Processing*, 129:407–436, August 2019.

[128] Hyuk Jeong and Jeong-Guon Ih. Implementation of a New Algorithm Using the STFT with Variable Frequency Resolution for the Time-Frequency Auditory Model. *Journal of the Audio Engineering Society*, 47(4):240–251, April 1999.

[129] Jin-Ho Bae, Jeong-Guon Ih, and Sang-Ryeol Kim. Precise order tracking analysis of time-varying vibro-acoustic signature from rotating machines. In *Proceedings of Meeting on Acoustics*, volume 19, pages 055076–055076, Montreal, Canada, 2013.

List of Related Publications

[MG1] Gabor Manhertz and Akos Bereczky. STFT Spectrogram Based Hybrid Evaluation Method For Rotating Machine Transient Vibration Analysis. *Mechanical Systems and Signal Processing*, 154:1–16, 2021.

[MG2] Gábor Manhertz and Ákos Bereczky. Development of a vibration expert system to analyze and predict malfunctions in internal-combustion engine. In *Proceedings of ARES '14*, pages 24–29, 2014.

[MG3] Gábor Manhertz, Dániel Modok, and Ákos Bereczky. Evaluation of short-time fourier-transformation spectrograms derived from the vibration measurement of internal-combustion engines. In *2016 IEEE International Power Electronics and Motion Control Conference (PEMC)*, pages 812–817, 2016.

[MG4] Gábor Manhertz, Dániel Modok, and Ákos Bereczky. Frekvenciakomponensek Követése Short-Time Fourier-Transzformáció Spektrogramon Képfeldolgozási Módszerekkel. In *Tavaszi Szél 2016 / Spring Wind 2016*, volume III, pages 239–250, 2016.

[MG5] Petra Balla, Gábor Manhertz, and Ákos Antal. Computerized Evaluation of Digital Orthopedic Moiré Pictures. *Recent Innovations in Mechatronics*, 1(1-2):1–7, 2014.

[MG6] Petra Balla, Gábor Manhertz, and Ákos Antal. Diagnostic moiré image evaluation in spinal deformities. *OPTICA APPLICATA; 03/2016; ISSN 1429-7507*, 2016.

[MG7] Petra Balla, Gábor Manhertz, and Ákos Antal. Spineline detection with image evaluation. *Recent Innovations in Mechatronics*, 2(1-2):1–8, 2015.

[MG8] Gábor Manhertz, Gábor Gárdonyi, and Gábor Pór. Managing measured vibration data for malfunction detection of an assembled mechanical coupling. *The International Journal of Advanced Manufacturing Technology*, 75(5):693–703, 2014.

[MG9] Gábor Manhertz and Ákos Antal. The effect of air-fuel equivalence ratio change on the vibration components of an internal-combustion engine. *Recent Innovations in Mechatronics*, 2(1-2):1–6, 2015.

[MG10] Gábor Manhertz. Légfelesleg-tényező változásának hatása belsőégésű motor rezgésösszetevőire. In *Tavaszi Szél 2014 / Spring Wind 2014*, volume VII, pages 446–459, 2014.

List of Figures

List of Tables